arXiv:1512.03994v2 [cond-mat.quant-gas] 25 Dec 2015

Mott insulating states and quantum phase transitions of correlated SU($2N$) Dirac fermions

Zhichao Zhou,[1] Da Wang,[2] Zi Yang Meng,[3] Yu Wang,[1,*] and Congjun Wu[4,†]

[1] *School of Physics and Technology, Wuhan University, Wuhan 430072, China*
[2] *National Laboratory of Solid State Microstructures and School of Physics, Nanjing University, Nanjing, 210093, China*
[3] *Beijing National Laboratory for Condensed Matter Physics, and Institute of Physics, Chinese Academy of Sciences, Beijing 100190, China*
[4] *Department of Physics, University of California, San Diego, CA 92093, USA*

The interplay between charge and spin degrees of freedom in strongly correlated fermionic systems, in particular of Dirac fermions, is a long-standing problem in condensed matter physics. We investigate the competing orders in the half-filled SU($2N$) Hubbard model on a honeycomb lattice, which can be accurately realized in optical lattices with large-spin ultra-cold alkaline-earth fermions. Employing large-scale projector determinant quantum Monte Carlo simulations, we have explored quantum phase transitions from the gapless Dirac semi-metals to the gapped Mott-insulating phases in the SU(4) and SU(6) cases. Both of these Mott-insulating states are found to be columnar valence bond solid (cVBS) and to be absent of the antiferromagnetic Néel ordering and the loop current ordering. Inside the cVBS phases, the dimer ordering is enhanced by increasing fermion components and behaves non-monotonically as the interaction strength increases. Although the transitions generally should be of first order due to a cubic invariance possessed by the cVBS order, the coupling to gapless Dirac fermions can soften the transitions to second order through a non-analytic term in the free energy. Our simulations provide important guidance for the experimental explorations of novel states of matter with ultra-cold alkaline earth fermions.

PACS numbers: 1.10.Fd, 02.70.Ss, 03.75.Ss, 37.10.Jk, 71. 27.+a

I. INTRODUCTION

Massless Dirac fermions, describing the low energy quasiparticles on the honeycomb lattice, have received a great deal of attention in the past decade due to the rapid progress in graphene-related and topological materials[1–4]. On the theoretical aspect, how the gapless fermions develop gap is an important scientific question both to condensed matter and high-energy physics[5,6]. In condensed matter systems, gap opening is often accompanied by symmetry breaking developing charge or spin orders. On the other hand, interaction can also open energy gap in the Mott insulating phase with or without spontaneous symmetry breaking. The simplest theoretical model describing the correlated electrons is the Hubbard model[7] which preserves the SU(2) symmetry. The studies of the SU(2) Hubbard model on the honeycomb lattice have shown a quantum phase transition from the massless Dirac semi-metal phase to a Mott insulating phase accompanied by the appearance of the long-range antiferromagnetic Néel ordering, even though whether these two transitions occur simultaneously is still under debate[8? –10].

One important question is the possible novel physics if fermions possess more than two internal components. In this case, the SU(2) Hubbard model can be generalized to the SU(2N) one[11–13]. (Since the fermion component number is typically even, we denote it $2N$ throughout this article.) This generalization is not only out of curiosity, but also can actually be implemented in the state-of-art cold atom experiments with large-spin alkaline-earth fermions[14–20]. These large-spin fermions are fundamentally different from the large-spin systems in solids which usually only exhibit the SU(2) symmetry. In contrast, the large-spin ultra-cold fermions provide a route to realize high symmetries without fine tuning[21]. As an early effort, the simplest large spin fermion systems with spin-$\frac{3}{2}$, including both alkali and alkaline-earth fermions were proved to be generically SO(5), or, isomorphically, Sp(4) symmetric without fine tuning[22–26]. For alkali-earth fermions, their interactions are spin-independent. Therefore, such systems naturally realize the SU($2N$) symmetry with $2N = 2I + 1$ and I the fermion hyperfine spin number, as observed in several recent cold atom experiments. Motivated by these theoretical and experimental progresses, the SU($2N$) Hubbard model has provoked our interest and been studied systematically in several recent works but only focusing on the square lattice[27–30]. These studies show that the full understanding of the SU($2N$) Hubbard models requires equal-footing treatments of both the small-U Slater physics and the large-U Mott physics.

The competition between the charge and spin degrees of freedom of the SU($2N$) Hubbard model is a challenging problem due to its non-perturbative nature. At half-filling and in the large-U limit, where charge fluctuations are suppressed, the low energy spin degrees of freedom are described by the SU($2N$) Heisenberg model with the super-exchange energy scale $J = 4t^2/U$[31,32], *i.e.*, each site is under the constraint of N fermions per site. The large-N expansion technique, in which $1/N$ is used as a perturbative parameter, has been applied to study the SU($2N$) Heisenberg model. The VBS states, also named as the dimer ordering states, were found on both the

square and honeycomb lattices for large enough N[33]. Recent quantum Monte Carlo (QMC) calculations show support to the large-N result and further identified the transition from VBS to the antiferromagnetic Néel order as N decreases[34–38]. In literature, a phenomenological t-J-$\tilde{U}$ model is often studied, in which $\tilde{U}$ is an effective onsite repulsion but the antiferromagnetic super-exchange J is put by hand[39]. At $\tilde{U}=0$, it becomes an unrestricted t-J model which has been studied by QMC on both the square lattice[40] and the honeycomb lattice[41]. In the latter, the long-range antiferromagnetic Néel order was found in the SU(2) case, while the plaquette VBS (pVBS) and the columnar VBS (cVBS) orders were identified in the SU(4) and SU($2N\geq 6$) cases, respectively.

However, the SU($2N$) Heisenberg model completely neglects charge fluctuations, while the unrestricted t-J model misses the essential Mott-physics originated from the onsite repulsion U. The values of J typically used in the unrestricted t-J model are overestimated compared to $J=4t^2/U$ arising from the 2nd order perturbation super-exchange process based on the Hubbard model. Therefore, both the Heisenberg model and the unrestricted t-J model cannot capture the rich competition and interplay between charge and spin degrees of freedom in the entire interaction region from the Dirac semi-metal phase to the Mott-insulating phase.

In this paper, we study the original SU($2N$) Hubbard model on the honeycomb lattice which correctly captures physics in both spin and charge channels. Therefore, our results go beyond those based on the SU($2N$) Heisenberg models and the unrestricted t-J model. Considering both the honeycomb optical lattice[42] and the SU($2N$) ultra-cold fermions are already experimentally realized, our simulations will provide helpful guidance for the future experimental study for exotic quantum states.

We employ the projector determinant QMC method which is free of the sign problem at half-filling[43–45]. The non-perturbative nature of the QMC method is capable of describing both charge fluctuations at intermediate interaction region and Mott-physics in the strong interaction region. As U increases, quantum phase transitions from the Dirac semi-metal phases to the Mott-insulating phases are identified for both SU(4) and SU(6) cases. The cVBS orders develop in the Mott insulating phases but both the antiferromagnetic Néel and current-loop orders are absent. The strength of the cVBS orders first grows and then drops in the large-U region due to the suppression of the overall kinetic energy scale. Meanwhile, both the single particle and spin gaps open in the cVBS phases. All these results can be understood as a consequence of the competition between the weak-U itinerant physics and large-U Mott physics. Since the cVBS and pVBS share the same order parameter except a π-phase difference, the transitions in general should be 1st order based on the Ginzburg-Landau analysis. Nevertheless, we also show that the transitions at zero temperature may be continuous 2nd order due to the coupling between the cVBS order and the gapless Dirac fermions.

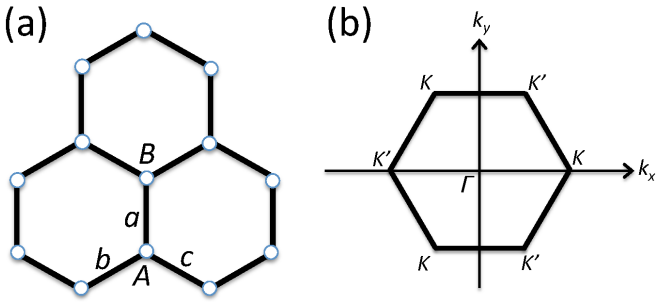

FIG. 1. a) The honeycomb lattice and the bond orientations. (b) The Brillouin zone. The Dirac points are located at $\vec{K}$ and $\vec{K}'$ at $(\pm\frac{4\pi}{3\sqrt{3}a_0},0)$. The three $\vec{K}(\vec{K}')$ points are equivalent to each other.

The rest of this paper is organized as follows. In Sect.II, the SU($2N$) Hubbard models are introduced, and possible VBS ordering patterns are analyzed. Throughout this article, we focus on two concrete examples with SU(4) and SU(6) symmetries. A new technique of distinguishing different VBS patterns is employed. Other parameters for QMC simulations are also presented. In Sect.III, transitions from the semi-metal phases to the Mott-insulating phases are studied by calculating the dynamical properties of the system, including both the single-particle gap and the spin gap. In Sect.IV, the competition between the Néel ordering and the cVBS ordering is studied. In Sect. V, the absence of the current loop ordering is shown. In Sect.VI, the nature of the phase transitions between the gapless Dirac semi-metal phase and the gapped cVBS phase is discussed. Conclusions are made in Sect.VII.

II. MODEL AND METHOD

A. SU($2N$) Hubbard model on honeycomb lattice

The honeycomb lattice is a bipartite but non-Bravais lattice. Each unit cell consists two sites belonging to the A and B-sublattices, respectively. Each site in the A-sublattice connects three bonds to its three B-neighbors denoted as a, b and c as shown in Fig. 1 (a). The Brillouin zone can be represented as a regular hexagon with the edge length $\frac{4\pi}{3\sqrt{3}a_0}$ as shown in Fig. 1 (b), where a_0 is the nearest-neighbor bond length. It is well-known that the single-particle spectra on the honeycomb lattice exhibit two gapless Dirac cones located at $\vec{K}$ and $\vec{K}'$, which is protected by the D_6 point group symmetry.

We employ the following SU($2N$) Hubbard model defined in the honeycomb lattice as

$$H=-t\sum_{i\in A,\hat{e}_j;\alpha}\left(c^{\dagger}_{i\alpha}c_{i+\hat{e}_j,\alpha}+h.c.\right)+\frac{U}{2}\sum_{i\in A\oplus B}\left(n_i-N\right)^2,$$

(1)

where $\hat{e}_j$'s with $j = a, b, c$ represent unit vectors along three bond orientations, respectively; α is the spin index taking values from 1 to $2N$; $n_i = \sum_\alpha c^\dagger_{i\alpha} c_{i\alpha}$ is the total particle number operator on site i; t is the hopping integral which is set as energy unit throughout the paper; U is the onsite Coulomb repulsion. Eq. 1 has already been set at the particle-hole symmetric point such that $\langle n_i \rangle = N$, thus the chemical potential does not appear explicitly. The convention of U is defined as follows: In the atomic limit of $t/U \to 0$, on the half-filled background, if a single particle is moved from one site to another, the excitation energy is U, independent of N.

The SU($2N$) generators on each site i are defined as

$$S_{\alpha\beta}(i) = c^\dagger_{i,\alpha} c_{i,\beta} - \frac{\delta_{\alpha\beta}}{2N} \sum_{\gamma=1}^{2N} c^\dagger_{i,\gamma} c_{i,\gamma}, \tag{2}$$

which satisfies the constraint of $\sum_\alpha S_{\alpha\alpha}(i) = 0$. Compared with the representation in terms of the Gellman matrix, the generators $S_{\alpha\beta}(i)$ satisfy the commutation relation in a simpler form as

$$[S_{\alpha\beta}(i), S_{\gamma\delta}(j)] = \delta_{ij} \left[\delta_{\beta\gamma} S_{\alpha\delta}(i) - \delta_{\alpha\delta} S_{\gamma\beta}(i)\right]. \tag{3}$$

The two-point equal-time SU($2N$) spin-spin correlation function is defined as

$$S_{spin}(i,j) = \sum_{\alpha,\beta} \langle S_{\alpha\beta}(i) S_{\beta\alpha}(j) \rangle, \tag{4}$$

where $\langle\rangle$ means the expectation value evaluated over the ground state. The staggered spin structure factor is defined as

$$S_{stag}(L) = \frac{1}{2L^2} \sum_{ij} (-1)^{i+j} S_{spin}(i,j), \tag{5}$$

where L is the linear system size and $2L^2$ is the number of lattice sites. The long-range Néel order is given by

$$M_{nl} = \lim_{L\to\infty} \sqrt{\frac{1}{2L^2} S_{stag}(L)}. \tag{6}$$

Next we analyze the possible VBS ordering pattern on the honeycomb lattice. Typically, there are three non-equivalent VBS configurations: columnar VBS (cVBS), plaquette VBS (pVBS), and the staggered VBS (sVBS) as depicted in Fig. 2 (a), (b), and (c), respectively. The s-dimer ordering still maintains the two-site unit cell. Among them, sVBS does not break translational symmetry but breaks the six-fold rotational symmetry down to two-fold. It shifts the locations of Dirac points away from $\vec{K}$ and $\vec{K}'$. The sVBS does not open gap unless its magnitude is comparable to t, thus it is not favored. The c- and pVBS orders exhibit the $\sqrt{3} \times \sqrt{3}$ structure, and their symmetry patterns are the same. They enlarge the unit cell to six sites but still maintain the six-fold rotational symmetry. Both the cVBS and pVBS orderings are at the wave vector $\vec{K}$ or $\vec{K}'$. Infinitesimal cVBS and

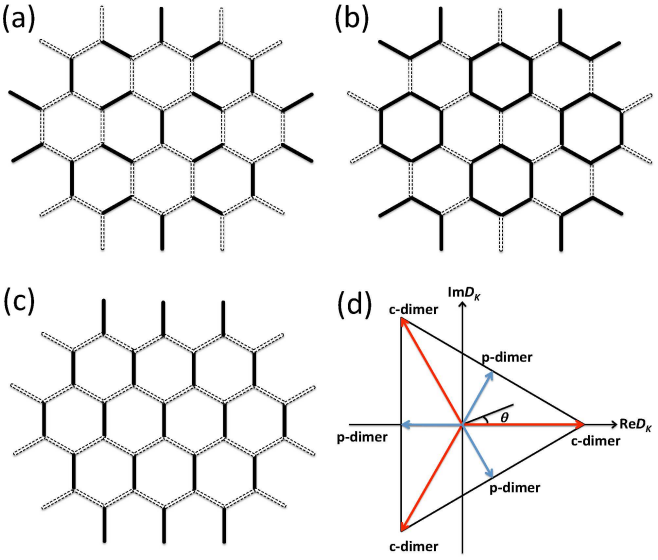

FIG. 2. Possible VBS configurations: (a) cVBS and (b) pVBS break translational symmetry and exhibit a $\sqrt{3} \times \sqrt{3}$ super-unit cell; (c) the sVBS configuration maintains translational symmetry. (d) The argument θ of the VBS order parameter $D_{K,1}$. The values of $\theta = 0, \frac{2}{3}\pi, \frac{4}{3}\pi$ represent the ideal cVBS order depicted in (a), and the values of $\theta = \pi, \frac{5}{3}\pi, \frac{1}{3}\pi$ represent the ideal pVBS order depicted in (b).

pVBS orders open the single particle gap and render the semi-metal with Dirac cones to an insulator. Below we will only consider the cVBS and pVBS orderings.

To distinguish different VBS dimer orderings, without loss of generality, we consider each site i of the A-sublattice and define its three nearest neighboring bonds $d_{i,\hat{e_j}}$ as

$$d_{i,\hat{e}_j} = \frac{1}{2N} \sum_{\alpha=1}^{2N} \left(c^\dagger_{i\alpha} c_{i+\hat{e}_j,\alpha} + h.c. \right), \tag{7}$$

where j represents the three bonds shown in Fig. 1 (a). Following Ref. 46, we define the complex order parameters $D_{K,m}$ with $m = 0, \pm 1$,

$$D_{K,m}(L) = \frac{1}{L^2} \sum_{i\in A} \left(d_{i,\hat{e}_a} + \omega^m d_{i,\hat{e}_b} + \omega^{2m} d_{i,\hat{e}_c} \right) e^{i\vec{K}\cdot\vec{r}_i}, \tag{8}$$

in which $\omega = e^{i\frac{2}{3}\pi}$, and $m = 0, \pm 1$. If we change $\vec{K}$ to $\vec{K}'$ in Eq. 8, it does not give rise to new orders since $D_{K,m} = D^*_{K',-m}$. The cases with $m = 0, -1$ correspond to the trimer orderings. $D_{K,m=1}$ corresponds to the p and c-dimer orderings. The difference between $m = \pm 1$ is because the phase factors in Eq. 8 are associated with $\vec{K}$ which already breaks the equivalence between the chiral indices $m = \pm 1$.

For simplicity, we define the following dimer strength parameter which only keeps correlations among bonds

along same directions as

$$\dim_K = \lim_{L\to+\infty} \frac{1}{L^2}\sqrt{\sum_{i,i'\in A;\hat{e}_j} e^{iK\cdot(r_i-r_{i'})}\langle d_{i,\hat{e}_j} d_{i',\hat{e}_j}\rangle}$$
$$= \lim_{L\to+\infty} \frac{1}{\sqrt{3}L^2}\sqrt{\sum_{m=0,\pm1} D^*_{K,m}(L)D_{K,m}(L)}. \quad (9)$$

As shown in Appendix E, the cases of $m = 0$ and -1 do not exhibit long-range ordering at half-filling. Then after the finite size scaling, $\dim_K$ actually represents the cVBS and pVBS orderings as

$$\dim_K = \lim_{L\to+\infty} \frac{1}{\sqrt{3}L^2}\sqrt{D^*_{K,1}(L)D_{K,1}(L)}. \quad (10)$$

Although the cVBS and pVBS states cannot be distinguished from the magnitudes of their common order parameter, the argument of the complex order parameter $D_{K,1}$ exhibits different patterns as shown in Fig. 2 (d). For example, for the ideal cVBS states, $\arg(D_{K,1}) = 0, \frac{2}{3}\pi$, or, $\frac{4}{3}\pi$, which are related to each other by translational or rotational symmetries. In contrast, for the ideal pVBS states, $\arg(D_{K,1}) = \pi, \frac{5}{3}\pi$, or, $\frac{1}{3}\pi$, which distribute inversion symmetrically with respect to those of the cVBS states. To see the difference between cVBS and pVBS more clearly, we define the following parameter

$$W = \int dzdz^* P(z,z^*)\cos 3\theta, \quad (11)$$

where $z = D_{K,1}$, $\theta = \arg(z)$, and $P(z,z^*)$ is the probability density appearing in the Monte-Carlo sampling satisfying $\int dzdz^* P(z,z^*) = 1$. For the ideal cVBS state, $W = 1$, while for the ideal pVBS state, $W = -1$.

B. Parameters of QMC simulations

We apply the zero temperature projector QMC (PQMC) method[45,47] in the determinant formalism[43]. To preserve translational symmetry, the honeycomb lattice is subject to periodic boundary condition in real space. The half-filled SU($2N$) Hubbard model is free of the minus-sign problem in bipartite lattices as shown in Appendix B.

The trial wave function is chosen as the ground state of the non-interacting part in Eq. 1 with a small flux added to break the degeneracy at the Dirac points[8]. The scalings of $\Delta\tau \to 0$ and $\beta \to \infty$ scaling of physical observables are performed in appendix G and appendix H, respectively. We find simulation parameters $\Delta\tau = 0.05$ and $\beta = 40$ for QMC are sufficient to give accurate ground state properties of the system. The measurements of physical observables are performed close to $\beta/2$ after the projection to the ground state. For a typical largest $L = 15$ system, we run 500 warm-up QMC steps, followed by at least 20 QMC bins with 700 measurements inside each bin. And for relatively smaller size, more warm-up steps and measurement steps are used.

III. QUANTUM PHASE TRANSITION BETWEEN MASSLESS DIRAC SEMI-METAL AND CVBS INSULATING PHASE

In this section, we study the quantum phase transitions from the semi-metal phase of Dirac fermions to the gapped insulating phases both for the SU(4) and SU(6) cases. To identify the transition, we focus on the single-particle gap Δ_{sp} and the spin gap Δ_σ as a function of interaction U.

Physics of the honeycomb lattice is very different from that in the square lattice, in both the weak and strong coupling limits. In the weak coupling regime, at half-filling, the honeycomb lattice possesses robust massless Dirac fermion spectrum and the interaction effects are weakened by the vanishing of density of states. On the other hand, the square lattice has Fermi surface nesting and van Hove singularities where the density of states diverges logarithmically. Hence, the square lattice system is unstable at infinitesimally small interaction and the single-particle gap Δ_{sp} opens from $U = 0^+$. The corresponding antiferromagnetic insulator is a typical Slater-type insulator with a spin-density-wave order[43]. In the strong coupling regime at $U \to \infty$, the Mott physics gives rise to a large gap as $\Delta_{sp} \approx \frac{U}{2}$[7]. The honeycomb lattice has the smallest coordination number $z = 3$ among all of the 2D lattices. Compared to the square lattice with $z = 4$, the charge excitations in the honeycomb lattice are more difficult to delocalize, and thus its Mott physics is more robust. In comparison, both the weak and strong coupling regimes in the honeycomb lattice are more extended in terms of U/t than in the square lattice. Hence, the intermediate coupling regime in the honeycomb lattice should be greatly suppressed.

A. Single-particle gap Δ_{sp}

We measure the single-particle gap Δ_{sp} in QMC to monitor the transition from the semi-metal to Mott insulator. Before presenting the QMC results, let us discuss an intuitive picture to obtain the critical U_c for the opening of the single particle gap[30]. Suppose that we start with the strong coupling limit and add one more fermion on a site. After turning on the hopping t, the extra charge hops to its nearest neighbors. The number of possible hopping processes are zN, thus the band width $W_b \approx 2zNt$. The single-particle gap decreases approximately as

$$\Delta_{sp} \approx \frac{U}{2} - \frac{W_b}{2} \approx \frac{U}{2} - zNt, \quad (12)$$

leading to $U_c/t \approx 2zN$. This argument yields the trend that the larger the fermion flavors $2N$, the stronger critical U_c is needed to open the Δ_{sp}, in an approximate linear way. This trend is qualitatively consistent with our QMC results.

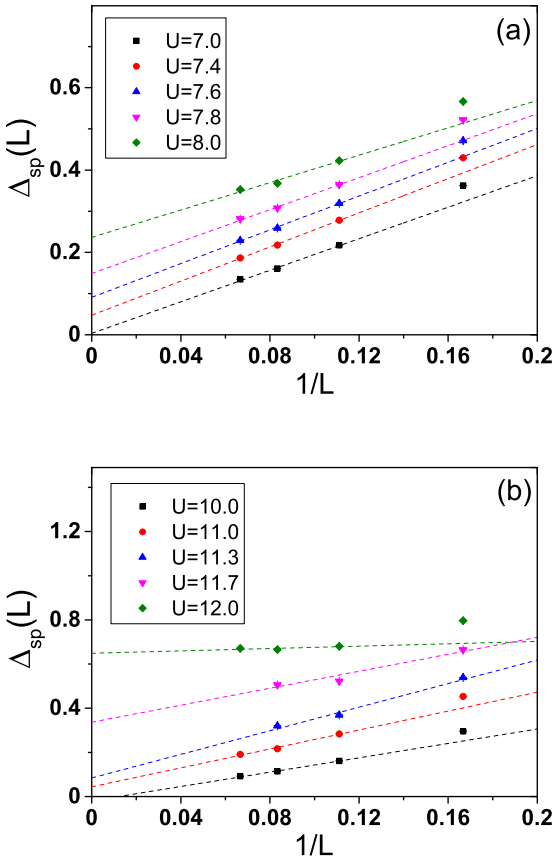

FIG. 3. Finite size scalings of the single-particle gap Δ_{sp} for (a) the SU(4) and (b) SU(6) Hubbard models with different values of U. The linear fitting is applied using the last three data points for each U. Error bars of the finite size Δ_{sp} are smaller than the symbols.

Since the minimal single-particle gap is located at the Dirac points $\vec{K}$ and $\vec{K}'$, we consider the imaginary-time displaced Green's function at $\vec{K}$ as

$$G(\vec{K},\tau) = \frac{1}{2L^2}\sum_{i,j\in A\oplus B} G(i,j,\tau)e^{i\vec{K}\cdot(\vec{r}_i-\vec{r}_j)}, \quad (13)$$

where

$$G(i,j,\tau) = \sum_{\alpha}\langle\Psi_G|c_{i,\alpha}(\tau)c^{\dagger}_{j,\alpha}(0)|\Psi_G\rangle, \quad (14)$$

and $|\Psi_G\rangle$ is the ground state. After a long imaginary-time displacement, the asymptotic behavior of $G(\vec{K},\tau)$ scales as $e^{-\tau\Delta_{sp}}$, and Δ_{sp} can then be obtained through fitting the slope of the $\ln G(\vec{K},\tau)$. In Appendix C, the raw data of $\ln G(\vec{K},\tau)$ are presented and the values of Δ_{sp} are extracted for different L. The finite size scalings of $\Delta_{sp}(L)$ in the SU(4) case for different U are presented in Fig. 3 (a). The critical interaction for the opening of Δ_{sp} is $U_c(2N=4)\approx 7$. For the SU(6) case, the same finite size scaling is presented in Fig. 3 (b), and Δ_{sp} becomes finite around $U_c(2N=6)\approx 10$. In contrast, in the SU(2) case, the critical value of $U_c(2N=2)\approx 3.7$ in literature[8,10].

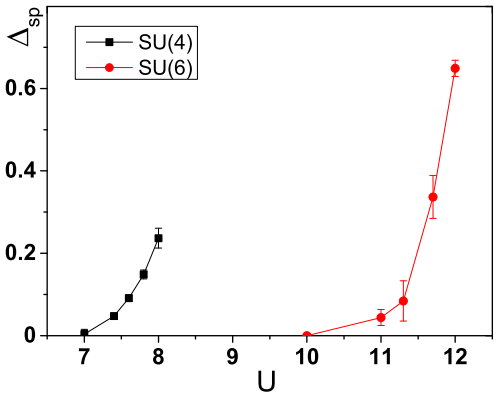

FIG. 4. The single particle gap Δ_{sp} *v.s.* U for the half-filled SU(4) and SU(6) Hubbard model in the honeycomb lattice.

The above QMC results show that with increasing $2N$, U_c also increases, exhibiting an approximate linear relation in agreement with the result based on Eq. 12. Nevertheless, Eq. 12 significantly overestimates the values of U_c compared with the accurate QMC results. The reason is that the charge excitations on the Mott insulating background are significantly incoherent, which suppresses the band width W_d in Eq. 12. This intrinsically many-body effect is beyond the single-particle picture as captured by the QMC simulations.

In Fig. 4, the relations Δ_{sp} *v.s.* U are plotted for both the SU(4) and SU(6) cases. It is more difficult to open the single-particle gap in SU(6) than SU(4). Nevertheless, Δ_{sp} increases more quickly in the SU(6) case after passing U_c. As will be seen in Sec. IV, the VBS order parameter $\dim_K$ is much stronger in the SU(6) case than in the SU(4) case. The enhancement of the VBS ordering suppresses the mobility of charge excitations, i.e., the band width W in Eq. 12. As a result, Δ_{sp} grows more quickly when U just passes U_c in the SU(6) case.

B. Spin gap Δ_σ

In order to further understand the nature of the gapped phases at $U > U_c$, spin gaps Δ_σ are calculated in both SU(4) and SU(6) cases. Before presenting QMC data, we can solve a two-site problem to understand the overall behavior of Δ_σ as varying U and N in the strong coupling regime. In this regime, the magnetic properties can be effectively described by the SU($2N$) Heisenberg model as

$$H^J_{ij} = \frac{J}{2}\sum_{\alpha\beta}\Big\{S_{\alpha\beta}(i)S_{\beta\alpha}(j) - \frac{1}{2N}n_i n_j\Big\}. \quad (15)$$

Since each site is half-filled, each SU($2N$) spin operator lies in the self-conjugate representation. The superexchange energy scales as $J = 4t^2/U$ at the 2nd order perturbation theory. After simple calculations, the ground state of this two-site problem is an SU($2N$) singlet with $E_0 = -\frac{N(N+1)}{2}J$, and the first excited state is in the SU($2N$) adjoint representation which is an analogue of the triplet excitation in the SU(2) case. The spin gap of this two-site problem can be calculated as

$$\Delta_\sigma \approx 4Nt^2/U, \tag{16}$$

which shows that Δ_σ is enhanced by increasing the fermion component number N, but suppressed by increasing U. Although Eq. 16 is only accurate for a single bond of two sites, it still can qualitatively yield an intuitive picture for Δ_σ in systems with VBS orderings in both SU(4) and SU(6) cases.

To extract the spin gap Δ_σ, we employ the imaginary-time displaced SU($2N$) spin-spin correlation function defined as

$$G_\sigma(\tau) = \frac{1}{2L^2}\sum_{i,j,\alpha,\beta}\Big\{(-1)^{i+j}\langle S_{\alpha\beta,i}(\tau)S_{\beta\alpha,j}(0)\rangle\Big\}. \tag{17}$$

Similar to the case of the single-particle gap, the value of the spin gap Δ_σ can be obtained by fitting $\ln G_\sigma(\tau)$. In Appendix D, the raw data of $\ln G_\sigma(\tau)$ are plotted and spin gaps are extracted.

The spin gap Δ_σ v.s. U at different system sizes L are presented in Fig.5 (a) and (b) for the SU(4) and SU(6) cases, respectively. At $U < U_c$, the systems are in the semi-metal phase, and thus the spin gaps vanish in the thermodynamic limit $L \to \infty$. In both the SU(4) and SU(6) cases, the relations of Δ_σ at finite size L v.s. U are non-monotonic: They reach maxima at values of U slightly larger than U_c, and after that, they decrease as U further increases, in agreement with intuitive understanding in Eq. 16. The positions of the peak in Δ_σ do not shift with L, and the Δ_σ converges quickly with L after passing the peak values, so the Fig. 5 (a) and (b) show that spin gaps are non-zero in thermodynamic limit for the gapped phase and there is no Néel order at $U > U_c$ (also see Sec. IV A below). The opening of Δ_σ at $U > U_c$ can be attributed to the developing of the VBS ordering as will be shown in Sect. IV B.

The behavior of the spin gap Δ_σ is also very different from the single-particle gap Δ_{sp}. The latter involves charge excitations while the former does not, thus the single-particle gap grows with U monotonically and approaches $\frac{U}{2}$ in the strong coupling limit. As analyzed in Sec. III A, the single-particle gap Δ_{sp} is weakened by increasing the fermion component number $2N$. In contrast, the spin gap is enhanced as shown in Eq. 16 in the strong coupling regime. Although in the strong coupling regime $\Delta_{sp} \gg \Delta_\sigma$, Δ_{sp} is comparable with Δ_σ in the intermediate coupling regime. This means that the spin and charge fluctuations are intertwined with each other, and there is no clear separation between them for low energy physics[8].

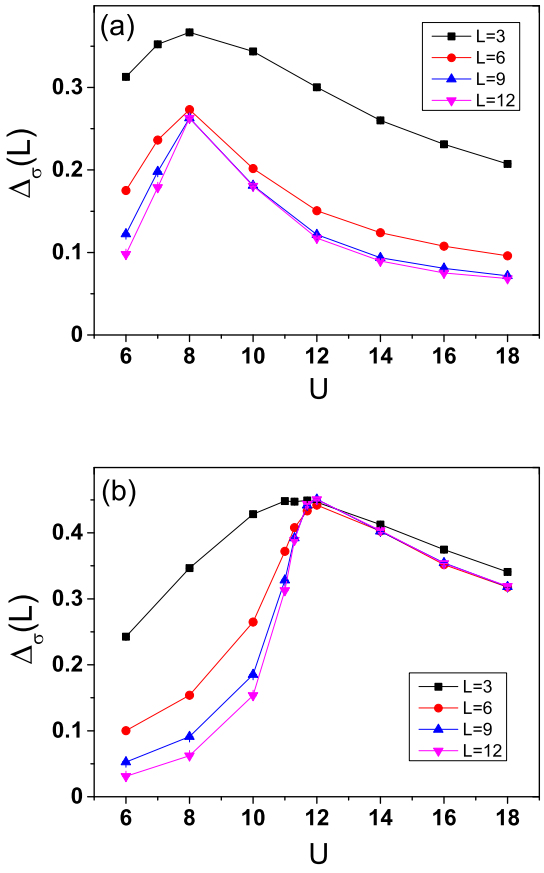

FIG. 5. Spin gap Δ_σ for finite size systems of the SU($2N$) Hubbard model in the honeycomb lattice: (a) the SU(4) case and (b) the SU(6) case. Error bars are smaller than the symbols.

IV. NÉEL V.S. VBS AS THE GROUND STATE

In this section we address the possible competition between the antiferromagnetic Néel order and the VBS dimer order, and explain why there is no Néel order as the ground state in the SU(4) and SU(6) cases at $U > U_c$.

Again, let us first discuss an intuitive picture to explain why increasing the fermion components favors the VBS order and suppresses the Néel order. We consider a two-site problem of a single bond in the strong coupling limit in which charge fluctuations can be neglected, and compare the energy gains for the Néel and SU($2N$) bond singlet configurations as depicted in Fig. 6. To maintain the Néel configuration, spin-flip process is not allowed. One fermion of a certain species on the left site can hop to the right, and then it must hop back. The total number of the virtual hopping processes is $2N$, and thus the energy gain at the 2nd order perturbation level is $2N\frac{t^2}{U}$. In contrast, if two sites form a SU($2N$) singlet, spin-flip processes are allowed and the energy gain is $2N(N+1)\frac{t^2}{U}$. Hence from the energy perspective, the

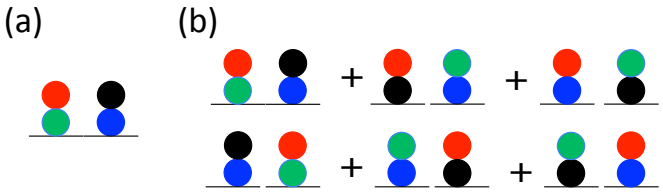

FIG. 6. (a) The classic Néel and (b) quantum dimer configurations across a bond for the case of $2N = 4$. In (a), fermion components on one site are 1 to N, and on the other site are $N + 1$ to $2N$. In (b), two sites form an SU($2N$) bond singlet. The exchange energy gain per bond in the Néel case is $2Nt^2/U$, and that for a singlet bond is $2N(N + 1)t^2/U$.

SU($2N$) singlet is the ground state over the Néel order, in the two-site problem. Of course, on the 2D lattice, situation becomes more complicated, the Néel state enjoys the advantage that every site can fit all of its neighbors, while for VBS one site can only participate in the formation of one singlet. But, roughly speaking, as $2N$ increases much larger than the coordination number z, we expect the VBS dimer order should win due to the enhanced quantum spin fluctuations[29,41]. On the contrary, the Néel order is expected to win at small N, such as in the SU(2) case[8–10].

A. The Néel order

Previous QMC results for the SU(2) case[8–10] showed that the Néel order is the ground state at large U. Our results of the SU(4) and SU(6) cases are quite different: the long-range Néel order is absent. The finite size scalings of the AF order parameter M_{nl} defined in Eq. 6 for the SU(4) and SU(6) cases are presented in Fig. 7 (a) and (b), respectively. For the SU(4) case, the finite size scaling on $M_{nl}(L)$ shows clear evidence of the vanishing of long-range Néel order at intermediate values from $U = 6$ to 14. The AF correlation is enhanced by further increasing U. At $U = 16, 18$, the finite-size scalings show very small residual values as $L \to \infty$. Nevertheless, it might well be an artifact of limited system sizes (L is up to 15). In particular, the curvatures of these $M_{nl}(L)$ curves are negative and thus it is conceivable that they will finally converge to zero as $L \to \infty$. And also in appendix F, we find there is no Néel order for large U cases by using pinning field method[10]. The situation in the SU(6) case is clearer: All the curves of $M_{nl}(L)$ exhibit a clear linear scaling in terms of $1/L$. We can safely conclude the absence of the long-range Néel order for all the values of U from 6 to 18.

In both SU(4) and SU(6) cases, long-range Néel order does not appear after the opening of the single-particle gap, which is in agreement with the developing of nonzero spin gaps. Compared to the Néel ordering in the SU(2) case in the honeycomb lattice, the larger values of $2N = 4, 6$ enhance quantum spin fluctuations. Let us compare with the result of SU($2N$) Hubbard model in the

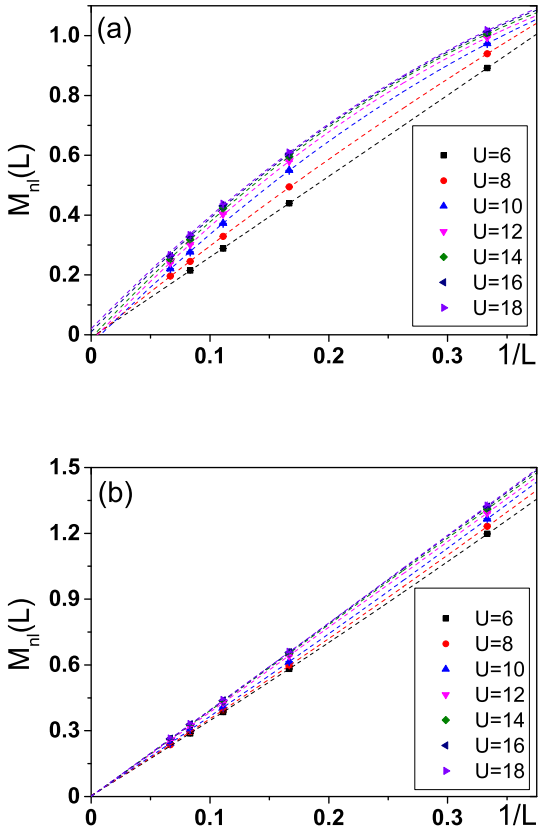

FIG. 7. The finite size scalings of the Néel order parameter M_{nl} against $1/L$ at different values of U: (a) the SU(4) case and (b) the SU(6) case. The quadratic polynomial fitting is used for L from 3 to 15. Error bars are smaller than symbols.

square lattice[29]. The Néel order remains robust in the SU(4) case for the entire parameter range of $0 < U < 20$ simulated. Although the Néel order is weakened at large values of U, it remains an open question whether it can persist to the limit of $U \to \infty$. As for the SU(6) case in the square lattice, the Néel order still appears in the weak and intermediate coupling regimes ($0 < U < 15$), and is replaced by the VBS dimer order in the strong coupling regime.

B. The VBS order

In this part, we show that although the Néel order is absent in the honeycomb lattice in both the SU(4) and SU(6) case, the VBS order appears after the single-particle gap opens.

The microscopic mechanisms of the VBS and Néel orders in the honeycomb lattice are different from those in the square lattice. In the square lattice, the Néel wave vector (π, π) matches the Fermi surface nesting condi-

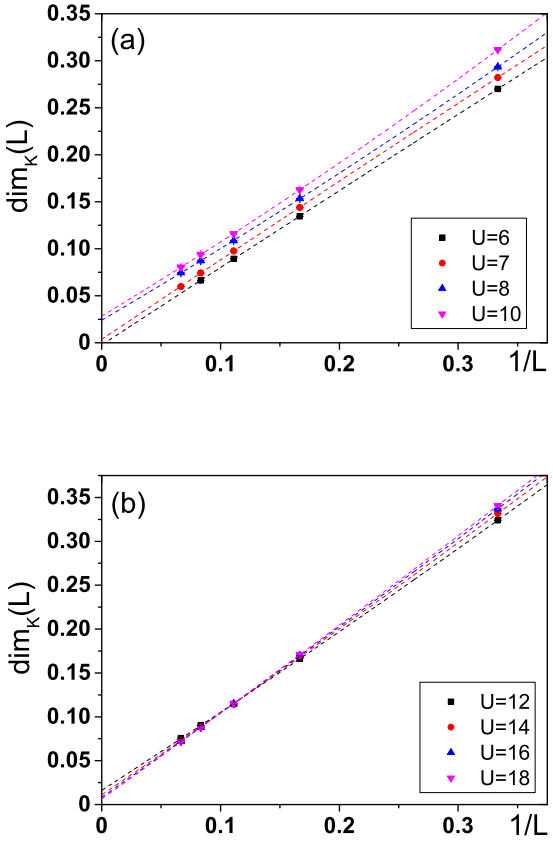

FIG. 8. Finite size scalings of $\dim_K(L)$ *v.s.* $1/L$ for the SU(4) Hubbard model: (*a*) $U = 6, 7, 8, 10$, and (*b*) $U = 12, 14, 16, 18$. The quadratic polynomial fitting is used, and error bars are smaller than symbols.

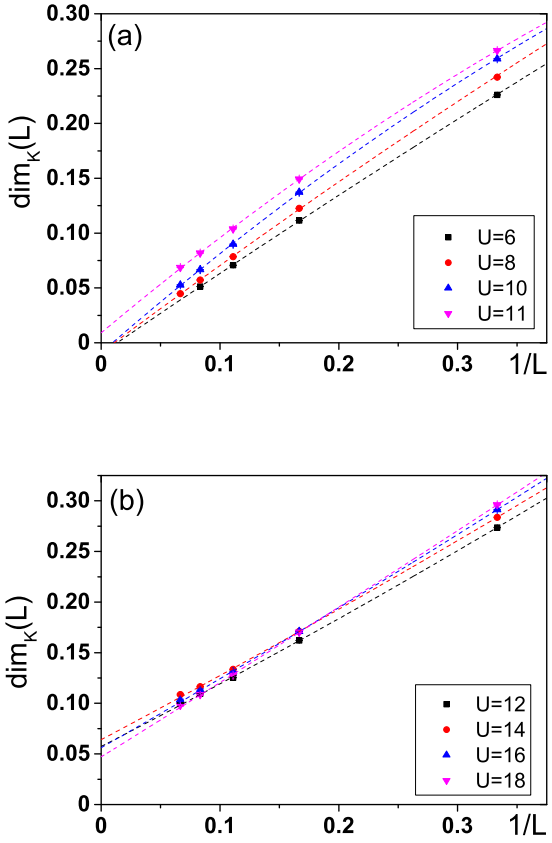

FIG. 9. Finite size scalings of $\dim_K(L)$ *v.s.* $1/L$ for the SU(6) Hubbard model: (*a*) $U = 6, 8, 10, 11$, and (*b*) $U = 12, 14, 16, 18$. The quadratic polynomial fitting is used, and error bars are smaller than symbols.

tion, while the cVBS wave vectors at $(\pi, 0)$ or $(0, \pi)$ do not. This explains why the Néel order wins over the VBS order in the weak and intermediate coupling regime for the SU(4) and SU(6) cases. The dimer ordering could win in the deep Mott insulating states in which the local moments rather than Fermi surfaces play the leading role. In contrast, in the honeycomb lattice the pVBS and cVBS orders break the translational symmetry. Their wave vectors connect two different Dirac points $\vec{K}$ and $\vec{K}'$ and can be viewed as a nesting between Fermi points. The Néel order does not break translational symmetry and generates gap within each Dirac point. Hence, in the honeycomb lattice, the Néel order has no particular advantage compared to the VBS order from the perspective of Fermi surface nesting.

The finite-size scalings of the VBS order parameter $\dim_K(L)$ of the SU(4) case are presented in Fig. 8. The long range VBS order starts to appear at $6 < U < 8$ as shown in Fig. 8 (*a*), which is consistent with the single-particle gap opening at $U_c \approx 7$. As further increasing U, the VBS order parameter in the $L \to \infty$ limit becomes non-monotonic: it keeps increasing until reaches the maximum around $U \approx 10$. After that, it begins to decrease as further increasing U as shown in Fig. 8 (*b*) for $U \geq 12$. In this case, the extrapolated values of $\dim_K(L)$ at $1/L \to 0$ are very weak. It is difficult to judge whether the VBS order vanishes. Nevertheless, the spin gap data in Fig. 5 (*a*) still show noticeable values, and thus are consistent with a weak VBS order.

The analysis for the SU(6) case can be carried out in parallel. The finite-size scalings of $\dim_K(L)$ are presented in Fig. 9 (*a*) and (*b*). The long-range order starts to appear at $U = 10 \sim 11$, which is consistent with the critical value of U_c for opening the single particle gap. Similar to the SU(4) case, the VBS order parameter in the $L \to \infty$ limit behaves non-monotonically as increasing U. The overall scale of the VBS order parameter in the SU(6) case is larger than that in the SU(4) case because the VBS order is strengthened by increasing $2N$.

Fig. 10 presents the extrapolated VBS order parameter as a function of U. With increasing U, the system undergoes a phase transition from the Dirac semi-

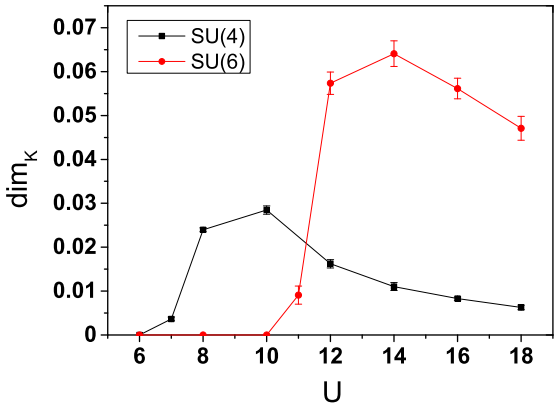

FIG. 10. The extrapolated VBS order parameter $\dim_K$ as a function of U for the SU(4) and SU(6) cases. The critical values of U_c for the appearances of the VBS order are consistent with those of the single-particle gap Δ_{sp} opening shown in Fig. 4.

metal phase to the VBS phase. The reason of the non-monotonic behavior of the VBS order parameter at $U > U_c$ is the following. The VBS order is essentially the spatial variation of the kinetic energy of each bond. For $U \approx U_c$, the system remains in the intermediate coupling regime. A dimerized bond in this regime is an SU($2N$) singlet state, but it is not the singlet based on the Heisenberg model Eq. 15: Each site has significant charge fluctuations, and the kinetic energy scale on each bond is at the order of t. In contrast, in the large-U limit, charge fluctuations are suppressed. The kinetic energy contributes through the 2nd order perturbation process, i.e., the super-exchange effect described by Eq. 15. The overall energy scale of the bond kinetic energy is suppressed to the order of t^2/U. Thus after the initial increase of the VBS order just after $U > U_c$, further increasing U reduces the overall kinetic energy scale, which suppresses the VBS order strength.

C. Nature of the VBS ordering pattern

As we explained in Sect. II A, both the cVBS and pVBS configurations exhibit the same symmetry breaking pattern. They are represented by the same complex order parameter $D_{K,1}$, and cannot be distinguished from the structural factor scalings which only yield magnitude of $D_{K,1}$. Nevertheless, the distributions of the argument angles are different between the cVBS and pVBS orders. We investigate the nature of the VBS order by calculating W following the definition in Eq. 11.

In Fig. 11 (a) and (b), we present the finite size scalings of W for the SU(4) and SU(6) cases, respectively. As mentioned below Eq. 11, $W = 1$ for a classic cVBS configuration, $W = -1$ for a classic pVBS configuration,

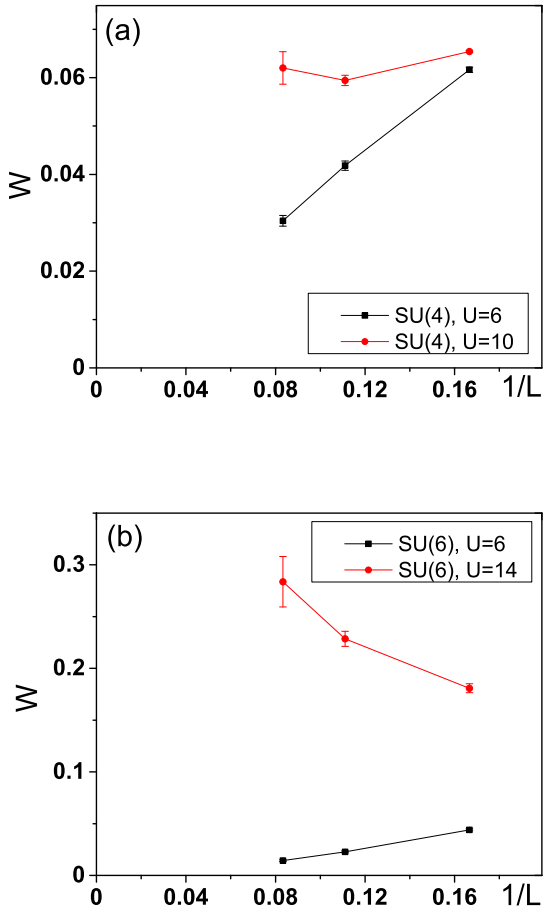

FIG. 11. Finite size scalings of W with different parameters U and $2N$: (a) SU(4) case with $U = 6, 10$, and (b) SU(6) case with $U = 6, 14$. The results clearly point out the VBS order at $U > U_c$ is cVBS.

and zero in the Dirac semi-metal phase. The finite size scalings of W indicate the most probable type of the VBS configuration. In both SU(4) and SU(6) cases, $U = 6$ lies in semi-metal phase, and thus W drops as increasing the lattice size.

For both cases of SU(4) with $U = 10$ and SU(6) with $U = 14$, the systems are in the VBS order phases. The finite-size scalings of W in Fig. 11 (a) and (b) show that they saturate to positive values indicating the cVBS instead of pVBS configuration. The values of W in the SU(6) are about one order higher than those in the SU(4) cases, indicating much stronger VBS order.

V. ABSENCE OF THE CURRENT ORDER

Besides the Néel and the VBS dimer orders discussed in the main text, a spontaneous current order provides

another possibility to open an energy gap for the SU($2N$) Dirac fermions. The effect of such current order (or loop currents) is similar to those give rise to the topological band structure in the spinless Haldane model[48], or, spin-1/2 Kane-Mele model[49]. In this section, we present the simulations on current orderings.

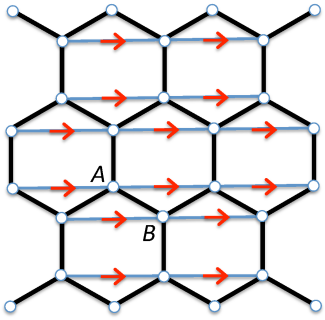

FIG. 12. The positive direction of current order on the honeycomb lattice.

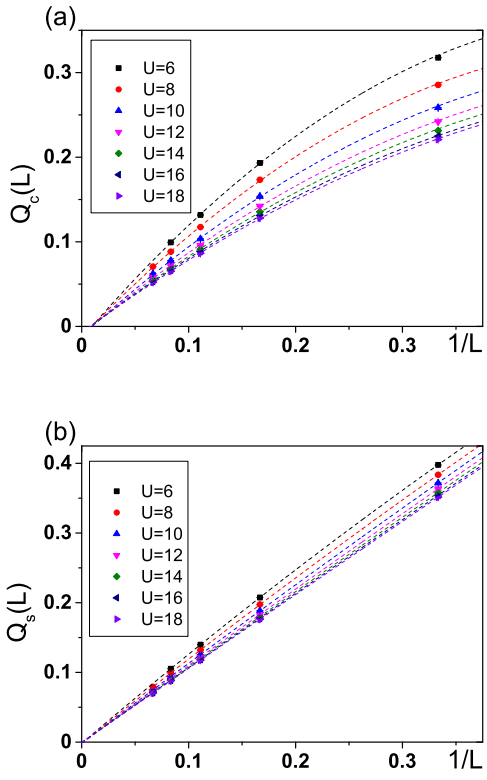

FIG. 13. The finite size scalings of the charge loop current order $Q_c(L)$ and spin loop current order $Q_s(L)$ for the SU(4) case. The quadratic polynomial fitting is used. Error bars of QMC data are smaller than symbols.

We define the following current operator for each fermion component α as

$$J^{\alpha}_{jj'} = i\left[\left(c^{\dagger}_{j,\alpha}c_{j',\alpha} - c^{\dagger}_{j',\alpha}c_{j,\alpha}\right)\right], \tag{18}$$

where jj' represent the next-nearest-neighbors and the positive direction of currents follows the arrows indicated in Fig. 12. For simplicity, we only consider the horizontal bonds. Furthermore, following Ref. [50], the charge and spin current order parameters are defined as

$$J^{c(s)}_{jj'} = \sum_{\alpha} F(\alpha) J^{a}_{jj'}, \tag{19}$$

where $F(\alpha) = \pm 1$ decides the current direction of the spin component α. We set $F(1, ..., 2N) = +1$ for J^c, while for spin current, $F(1, ..., N) = +1$ and $F(N + 1, ..., 2N) = -1$ without loss of generality. Then the loop current structure factors are defined as

$$Q_{c(s)} = \lim_{L\to\infty} \frac{1}{2L^2}\sqrt{\sum_{jk}(-1)^{j+k} J^{c(s)}_{jj'} J^{c(s)}_{kk'}}. \tag{20}$$

The simulation results are shown in Fig. 13 and Fig. 14 for the SU(4) and SU(6) cases, respectively. In both cases, both long-range charge and spin loop current orders are absent in the thermodynamic limit, excluding the possibility of spontaneous current orders as the cause of the gap opening in both the SU(4) and SU(6) cases.

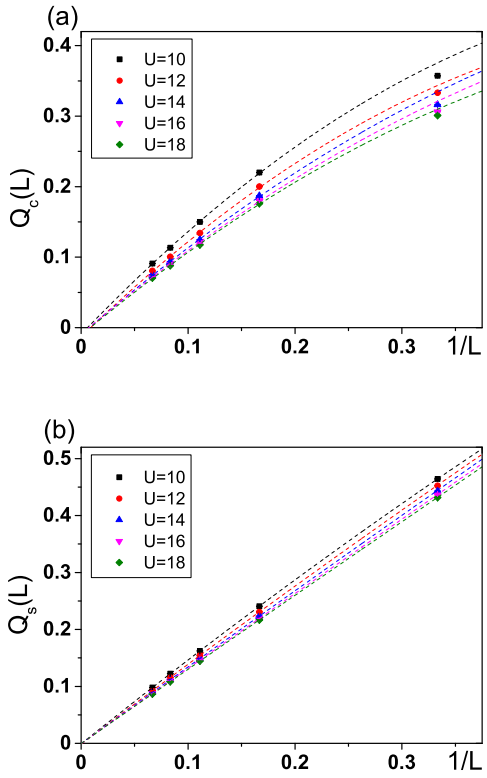

FIG. 14. The same as Fig. 13 but for the case of SU(6) and with different values of U.

VI. DISCUSSION ON THE NATURE OF THE DIRAC-TO-CVBS TRANSITION

From the above QMC analysis, we have identified the quantum phase transition between the Dirac semi-metal phase and the cVBS phase as U increases in both SU(4) and SU(6) cases. As discussed previously, the order parameter $D_{\vec{K},1}$ unifies two different VBS patterns: the cVBS and pVBS, which correspond to positive and negative values of $D_{\vec{K},1}$, respectively. This means that positive and negative values of $D_{\vec{K},1}$ are non-equivalent to each other. As a result, in principle, the cubic order terms $D^3_{\vec{K},1}$ and $D^{3,*}_{\vec{K},1}$ are allowed by symmetry in the effective action of the VBS state. Based on the Ginzburg-Landau (GL) theory, such odd order terms generally lead to first order phase transitions. However, we do not find strong evidence of first order phase transitions in our QMC simulations. This may be caused by a suppression of the third order terms by the coupling to the critical fluctuations of Dirac fermions close to the quantum phase transition point as analyzed below.

A. The Ginzburg-Landau analysis

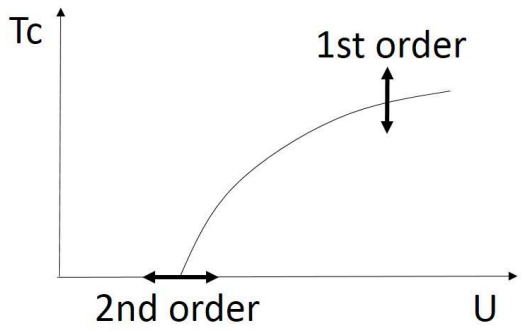

FIG. 15. Putative phase diagram of the Dirac semi-metal-to- cVBS phase transition on the honeycomb lattice. The zero temperature transition can be of the 2nd order due to the coupling to the gapless Dirac fermions, while the finite temperature transition should generally be of the 1st order.

In order to describe the Dirac semi-metal-to-VBS transition, we construct the following GL free energy density $f(\psi,\psi^*)$ where ψ is the gap function associated with the cVBS order $D_{\vec{K},1}$ which carries the energy unit. f does not possess the symmetry $\psi\to-\psi$, but needs to maintain the lattice translation symmetry. Based on the fact that ψ and ψ^* carry momenta $\pm\vec{K}$, respectively, the analytic part of the GL free energy is constructed as

$$f_A(\psi,\psi^*)=r_2|\psi|^2-r_3(\psi^{*3}+\psi^3)+r_4|\psi|^4. \quad (21)$$

The appearance of the r_3-terms is due to the lattice momentum conservation $3\vec{K}\equiv 0$ in the honeycomb lattice. The r_3-terms ensure the non-equivalence between cVBS ($\psi^3>0$) and pVBS ($\psi^3<0$). Based on the QMC results, the cVBS state wins over the pVBS state, thus $r_3>0$. According to the GL theory, the r_3-terms lead to the 1st order phase transition. At $r_{2t}=r_3^2/r_4$, there exist 4-degenerate energy minima located at $\psi=0$ and $\psi=\frac{r_3}{r_4}e^{i\theta}$ with $\theta=0,\pm\frac{2}{3}\pi$, respectively. The former minimum corresponds to disordered state, while the latter three minima correspond to the cVBS state. As r_2 is lowered below r_{2t}, the ground state configuration changes from the disordered semi-metal phase to the cVBS state discontinuously.

The above 1st order phase transition could be weak if $r_3/r_4\ll 1$. A continuous phase transition is recovered in the limit of $r_3/r_4\to 0$. The value of r_3 and r_4 can be estimated by considering their physical processes as follows. Since ψ carries momentum K, the dominant contribution to r_3 comes from the scattering processes of $K\to K'\to\Gamma\to K$ and $K\to\Gamma\to K'\to K$ where K,K' and Γ represent small regions centered around these momenta, respectively. The involvement of the high energy point Γ strongly reduces the value of r_3, which should be proportion to the inverse of the band width at the scale of $1/t$. On the other hand, with similar analysis to the r_4 term, the dominant scattering processes correspond to $K\to K'\to K\to K'\to K$, all of which are in the low energy region. Therefore, r_3/r_4 is expected to be small.

So far, we only consider the analytic part of the GL free energy in Eq. 21. Due to the coupling between ψ with the gapless fermions, the free energy potentially contains a non-analytic part even at the mean-field level as analyzed below. In our system, there exist $4N$ low energy Dirac cones. After the developing of the cVBS order, the single particle spectrum around each Dirac point at the mean-field level becomes $E_k=\sqrt{v^2k^2+|\psi|^2}$, where $\vec{k}$ is the deviation from the location of the Dirac point. We can estimate the free energy density at the mean-field level arising from the low energy spectra around the Dirac points as

$$f_L\approx-\frac{4N}{\beta}\int_0^\Lambda\frac{d^2\vec{k}}{(2\pi)^2}\left(\ln(1+e^{\beta E_k})+\ln(1+e^{-\beta E_k})\right)+\frac{1}{2Ng}|\psi|^2, \quad (22)$$

where Λ is the momentum cut-off, and β is the inverse of temperature. If taking the zero temperature limit first, i.e., $\beta\to\infty$, and then taking the limit of $|\psi|\to 0$, after performing the integral, we arrive at a non-analytic part not included in Eq. 21,

$$f_n=r_{3,n}|\psi|^3, \quad (23)$$

where $r_{3,n}=\frac{2N}{3\pi v^2}>0$. If $r_{3,n}>r_3$, then $r_{3,n}$ and r_3-terms combine together are positive definite, which cannot induce 1st order transition. If $r_{3,n}<r_3$, the first order phase transition remains but is weakened.

Since the semi-metal-to-cVBS transition only breaks discrete symmetry, it is expected to survive at finite temperatures. There exists an additional contribution at a

finite temperature from Eq. 22, which can be organized as

$$f_L(T) - f_L(T=0) = -\frac{4N}{\pi\beta^3}\int_{\beta|\psi|}^{+\infty} y\ln(1+e^{-y})dy, \tag{24}$$

where the upper limit of the integrand is set to $+\infty$. If we take the limit of $|\psi| \to 0$ first and then set β at an arbitrarily low but still finite temperature, the above expression contributes an extra non-analytic term

$$\Delta f_n(T) = -r_{3,n}|\psi|^3, \tag{25}$$

which precisely cancels f_n at zero temperature. As a result, the non-analytic part of the free-energy disappears at finite temperature. Thus finite temperature transition from the Dirac semi-metal-to-cVBS still remains the 1st order.

The above analysis shows that the low energy Dirac fermions can significantly changes the nature of the quantum phase transition through non-analytic contributions to the G-L free energy. Nevertheless, this effect can only exist at zero temperature quantum phase transition, not at finite temperature phase transition, as summarized in Fig. 15. In Sect. VI B, we perform a numeric study based on the mean-field theory, which agrees with the above analytic results.

Nevertheless, the above analysis is only at mean-field level. The strong quantum fluctuations due to the coupling between the VBS order and the gapless Dirac fermions may further soften the 1st order transition and drive the transition to be continuous. If this is true, it means that in the correlated SU($2N$) Dirac fermion systems, an exotic continuous quantum phase transition beyond typical GL paradigm is realized. Within the accuracy of the current QMC simulations, we cannot judge the nature of the Dirac semi-metal-to-cVBS transitions at the SU(4) and SU(6) cases are of weak 1st order or continuous 2nd order. We leave the further theoretical and numerical analyses to future works, but hope the conclusion by now is strong enough to motivate ultracold atom experiments to realize such exotic quantum phase transition.

B. A Mean-field theory calculation

In this part, we present a numeric solution to the mean-field theory at both finite and zero temperatures to illustrate the nature of the above transitions. Instead of directly using the Hubbard model, we employ a phenomenological model exhibiting the order parameter $D_{\vec{K},1}$ in the cVBS channel with the following interaction term

$$H_I = -g\sum_i D_{i,1}^\dagger D_{i,1}, \tag{26}$$

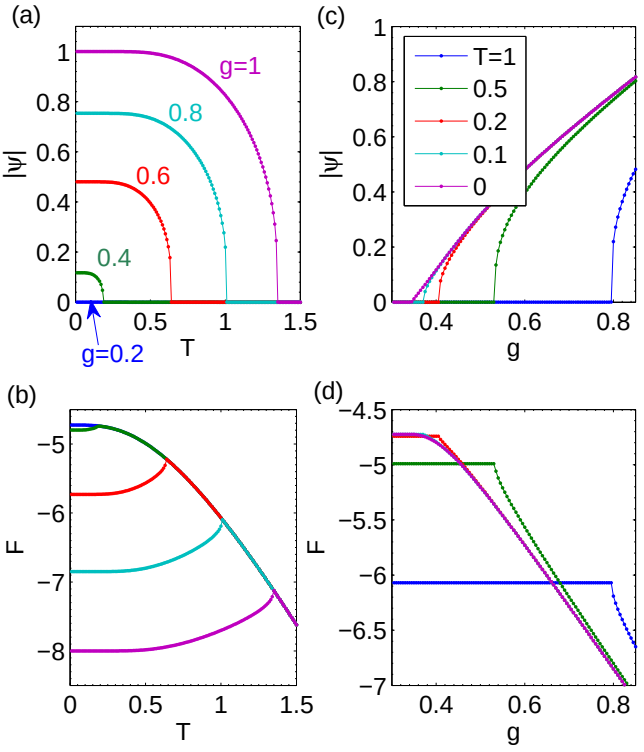

FIG. 16. Self-consistent mean field calculation results. In (a) and (b), the VBS order parameter $|\psi|$ and free energy F are plotted as a function of the temperature T. In (c) and (d), $|\psi|$ and F are plotted vs the effective interaction g. Linear lattice size $L = 99$ is used for finite $T \geq 0.01$, while larger $L = 300$ is used in the $T = 0$ case in order to eliminate the finite size effect.

where $g > 0$ is the effective interaction and $D_{i,1} = D_{\vec{K},1}\exp(i\vec{K}\cdot r_i)$. In the mean-field approximation,

$$H_I \approx -\sum_i \left[\left(D_{i,1}^\dagger \psi e^{i\vec{K}\cdot r_i} + h.c.\right) - \frac{1}{g}\psi^*\psi\right], \tag{27}$$

where $\psi = g\langle D_{\vec{K},1}\rangle$.

After Fourier transformation, the mean field Hamiltonian is

$$H_{MF} = \sum_{\vec{k}}\left[\left(\Psi_{\vec{k},a}^\dagger h_{\vec{k}}\Psi_{\vec{k},b} + h.c.\right) + \frac{1}{g}\psi^*\psi\right], \tag{28}$$

where $\Psi_{\vec{k},a|b} = [c_{\vec{k},a|b}, c_{\vec{k}+\vec{K},a|b}, c_{\vec{k}-\vec{K},a|b}]^t$ and the matrix kernel $h_{\vec{k}}$ is

$$h_{\vec{k}} = \begin{bmatrix} f_{\vec{k}} & -\psi f_{\vec{k}-\vec{K}} & -\psi^* f_{\vec{k}+\vec{K}} \\ -\psi^* f_{\vec{k}-\vec{K}} & f_{\vec{k}+\vec{K}} & -\psi f_{\vec{k}} \\ -\psi f_{\vec{k}+\vec{K}} & -\psi^* f_{\vec{k}} & f_{\vec{k}-\vec{K}} \end{bmatrix}, \tag{29}$$

in which $f_{\vec{k}} = \sum_j \exp(i\vec{k}\cdot\hat{e}_j)$. The value of ψ can be solve self-consistently through definition

$$\psi = \frac{g}{L^2}\sum_{\vec{k}}\left[f_{\vec{k}-\vec{K}}\langle c_{\vec{k}+\vec{K},a}^\dagger c_{\vec{k},b}\rangle + f_{\vec{k}-\vec{K}}^*\langle c_{\vec{k}+\vec{K},b}^\dagger c_{\vec{k},a}\rangle\right],$$

(30)

where $\exp(i\vec{K}\cdot\hat{e}_j)=\{1,\omega,\omega^*\}$ has been used to arrive at the above self-consistent relation.

The self-consistent results are shown in Fig. 16. At finite temperature $T>0$, the jumps of $|\psi|$ at critical points T_c and V_c indicate a first order phase transition, which is more obvious as shown by the cusps in the free energy data at transitions. However, as temperature decreases, the free energy as a function of V exhibits more smooth behavior, as shown in Fig. 16(d). Meanwhile, the discontinuous behavior $|\psi|$ at V_c becomes weaker and weaker and finally vanishes, resulting in a continuous quantum phase transition at zero temperature.

VII. CONCLUSIONS

Based on all the simulations and analysis above, we present a ground-state phase diagram of the SU($2N$) Hubbard model on the honeycomb lattice with $2N=4,6$. Quantum phase transitions from the Dirac semi-metal phases to the Mott insulating phases with increasing U are realized. The transition values of U_c increase with the number of fermion components $2N$. The Mott-insulating phases exhibit the cVBS order in the SU(4) and SU(6) cases in contrast to the antiferromagnetic Néel order previously studied in the SU(2) case[8–10]. The VBS signal is weak for SU(4) comparing with SU(6). Close to U_c, the cVBS order increases sharply, and it is suppressed as U further increases, due to the suppression of the overall kinetic energy scale in the strong Mott-insulating region. The nature of the semi-metal-to-cVBS transition is analyzed at the mean-field level, which can be of the 2nd order at zero temperature due to coupling to gapless Dirac fermions but still remains at the 1st order at finite temperatures.

Note added- Upon finishing the revised (2nd) version, we became aware of the interesting work by Li *et. al*[51] in which the continuous quantum phase transitions from the semi-metal phase to the cVBS phase are proposed and analyzed.

ACKNOWLEDGMENTS

Z. Z., Y. W., and C. W. gratefully acknowledge financial support from the National Natural Science Foundation of China under Grant Nos. 11574238 and 11328403, and the Fundamental Research Funds for the Central Universities. D. W. acknowledges the support from National Natural Science Foundation of China (11504164). C. W. is supported by the NSF DMR-1410375 and AFOSR FA9550-14-1-0168. C. W. acknowledges the support from the Presidents Research Catalyst Awards of University of California. Z. Y. M. is supported by the National Natural Science Foundation of China (Grant Nos. 11421092 and 11574359) and the National Thousand-Young-Talents Program of China.

Appendix A: Exact discrete Hubbard-Stratonovich transformation for the SU(4) and SU(6) Hubbard interactions

For the SU(2) Hubbard model, the discrete HS decomposition can be performed exactly[52]. For more complicated interactions and more flavors of spins such as in the SU($2N$) t-J or Hubbard models, the interaction terms are often decomposed into a set of discrete Ising fields with an systematic error at the order of $(U\Delta\tau)^4$[40,47]. This can be improved by an exact HS transformation for the SU($2N$) Hubbard model studied here, which is particularly useful at large values of U.

According to Ref. 29, the exact HS transformation for SU(4) and SU(6) Hubbard interaction is expressed as

$$e^{-\frac{\Delta\tau U}{2}(n_j-N)^2}=\frac{1}{4}\sum_{l=\pm1,\pm2}\gamma_j(l)e^{i\eta_j(l)(n_j-N)}, \tag{A1}$$

which employs two sets of discrete HS fields γ and η. For the cases of $2N=4$ and 6, the Ising fields take values of

$$\begin{aligned}
\gamma(\pm1)&=\frac{-a(3+a^2)+d}{d},\\
\gamma(\pm2)&=\frac{a(3+a^2)+d}{d},\\
\eta(\pm1)&=\pm\cos^{-1}\left\{\frac{a+2a^3+a^5+(a^2-1)d}{4}\right\},\\
\eta(\pm2)&=\pm\cos^{-1}\left\{\frac{a+2a^3+a^5-(a^2-1)d}{4}\right\},
\end{aligned}$$

where $a=e^{-\Delta\tau U/2}$, $d=\sqrt{8+a^2(3+a^2)^2}$.

Appendix B: Zero temperature QMC and absence of the sign problem at half-filling

In this appendix, we briefly introduce the zero temperature determinant QMC algorithm[45] and prove the absence of the sign problem for the half-filled SU($2N$) Hubbard model in bipartite lattices.

The Hamiltonian is composed of kinetic and interaction parts

$$H=H_K+H_I. \tag{B1}$$

The free part reads

$$H_K=\sum_{i,j,\alpha}c^\dagger_{i,\alpha}K_{i,j}c_{j,\alpha}, \tag{B2}$$

where K is the kinetic energy matrix and $\alpha=1,\cdots,2N$. The interaction part is

$$H_I=\frac{U}{2}\sum_i(n_i-N)^2, \tag{B3}$$

where $n_i = \sum_\alpha c^\dagger_{i\alpha} c_{i\alpha}$.

The expectation value of a physical observable operator $\hat{O}$ at zero temperature is defined as

$$\langle \hat{O} \rangle = \frac{\langle \psi_0 | \hat{O} | \psi_0 \rangle}{\langle \psi_0 | \psi_0 \rangle} = \frac{\langle \psi_T | e^{-\Theta H} \hat{O} e^{-\Theta H} | \psi_T \rangle}{\langle \psi_T | e^{-2\Theta H} | \psi_T \rangle}, \quad \text{(B4)}$$

where $|\psi_0\rangle$ is the ground state; Θ is a projection parameter large enough to ensure the trial wave function $|\psi_T\rangle$ is projected to the ground state $|\psi_0\rangle$. In our QMC simulations, we rename $2\Theta = \beta$ due to the similarity between projector QMC and finite temperature QMC algorithms.

Since H_K and H_I are non-commutative, we perform the second order Suzuki-Trotter decomposition

$$\mathrm{e}^{-\Delta\tau(H_K+H_I)} = \mathrm{e}^{-\Delta\tau H_K/2} \mathrm{e}^{-\Delta\tau H_I} \mathrm{e}^{-\Delta\tau H_K/2} + o[(\Delta\tau)^3], \quad \text{(B5)}$$

to divide Θ into M slices with discrete time interval $\Delta\tau = \Theta/M$. Then for each time slice, the discretized HS transformation of the interaction term Eq. B3 is performed in the density channel the same as that in Eq. A1. The imaginary time propagator, i.e., the projection operator, is represented as

$$e^{-\Theta H} = \sum_{\{l\}} \left\{ U_{\{l\}}(\Theta, 0) \prod_{i,p} \frac{\gamma_{i,p}(l)}{4} e^{-i\eta_{i,p}(l)N} \right\}, \quad \text{(B6)}$$

where

$$U_{\{l\}}(\Theta, 0) = \prod_{\alpha=1}^{2N} \prod_{p=M}^{1} e^{-\Delta\tau \sum_{i,j} c^\dagger_{i\alpha} K_{ij} c_{j\alpha}} e^{i \sum_i c^\dagger_{i\alpha} \eta_{i,p}(l) c_{i\alpha}}.$$

Here, $\gamma_{i,p}(l)$ and $\eta_{i,p}(l)$ are the space-time discretized HS fields defined in Eq. A1 with l taking values of $\pm 1, \pm 2$; $\sum_{\{l\}}$ represents the summation over the spatial and temporal configurations of the HS field; $U_{\{l\}}(\Theta, 0)$ is the propagation operator for the HS configuration $\{l\}$.

The trial wave function $|\psi_T\rangle$ is required to be a Slater determinant, which we will specify later. Substituting Eq. B6 into Eq. B4, we obtain

$$\langle \hat{O} \rangle = \frac{\sum_{\{l\}} \left\{ \langle \psi_T \ | U_l(2\Theta, \Theta) \ \hat{O} \ U_l(\Theta, 0) | \psi_T \rangle \prod_{i,p} \gamma_{i,p}(l) e^{-i\eta_{i,p}(l)N} \right\}}{\sum_{\{l\}} \left\{ \langle \psi_T | U_l(2\Theta, 0) | \psi_T \rangle \prod_{i,p} \gamma_{i,p}(l) e^{-i\eta_{i,p}(l)N} \right\}} = \sum_{\{l\}} P_{\{l\}} \ \langle \hat{O} \rangle_{\{l\}}, \quad \text{(B7)}$$

where $\langle O \rangle_{\{l\}}$ is the average value of $\hat{O}$ for the space-time HS configuration $\{l\}$ defined as

$$\langle O \rangle_{\{l\}} = \frac{\langle \psi_T | U_{\{l\}}(2\Theta, \Theta) \ \hat{O} \ U_{\{l\}}(\Theta, 0) | \psi_T \rangle}{\langle \psi_T | U_{\{l\}}(2\Theta, 0) | \psi_T \rangle}, \quad \text{(B8)}$$

and $P_{\{l\}}$ is the corresponding probability of the HS field configuration $\{l\}$ as

$$P_{\{l\}} = \frac{1}{Z} \ \langle \psi_T | U_l(2\Theta, 0) | \psi_T \rangle \prod_{i,p} \gamma_{i,p}(l) e^{-i\eta_{i,p}(l)N}. \quad \text{(B9)}$$

Z is defined as

$$Z = \sum_{\{l\}} \langle \psi_T | U_l(2\Theta, 0) | \psi_T \rangle \prod_{i,p} \gamma_{i,p}(l) e^{-i\eta_{i,p}(l)N} \quad \text{(B10)}$$

The summation over the HS configurations $\{l\}$ can be done by the Monte Carlo method.

Next we prove the absence of the sign problem for the SU($2N$) Hubbard model at half-filling in the zero temperature QMC method, *i.e.*, the probability $P_{\{l\}}$ is positive-definite. We factorize the trial wave function as $|\Psi_T\rangle = \otimes_{\alpha=1}^{2N} |\psi_T^{N_\alpha}\rangle$, where $|\psi_T^{N_\alpha}\rangle$ is a Slater-determinant state for spin-α electrons with the particle number N_α. Then $P_{\{l\}}$ reads as

$$P_{\{l\}} = \frac{1}{Z} \left[\prod_{\alpha=1}^{2N} \langle \psi_T^{N_\alpha} | \prod_{p=2M}^{1} e^{-\Delta\tau \sum_{i,j} c^\dagger_{i\alpha} K_{ij} c_{j\alpha}} e^{i \sum_i \eta_{i,p}(l)(c^\dagger_{i\alpha} c_{i\alpha} - \frac{1}{2})} \ | \psi_T^{N_\alpha} \rangle \right] \left[\prod_{i,p} \gamma_{i,p}(l) \right], \quad \text{(B11)}$$

where the HS fields $\gamma_{i,p}(l)$ given by Eq. A1 are positive-definite.

Let us perform a particle-hole transformation only to the spin-$\alpha = N+1, \cdots, 2N$ component

$$c^\dagger_{i\alpha} \to d_{i\alpha} = (-1)^i c^\dagger_{i\alpha}, \ c_{i\alpha} \to d^\dagger_{i\alpha} = (-1)^i c_{i\alpha}, \quad \text{(B12)}$$

then the Slater-determinant state $|\psi_T^{N_\alpha}\rangle$ changes to another Slater-determinant state of holes with the hole number $N_L - N_\alpha$ denoted as $|\psi_T^{h,N_L-N_\alpha}\rangle$. We arrive at

$$P_{\{l\}} = \frac{1}{Z}\prod_{\alpha=1}^{N}\langle\psi_T^{N_\alpha}|\prod_{p=2M}^{1} e^{-\Delta\tau\sum_{i,j}c_{i\alpha}^\dagger K_{ij}c_{j\alpha}} e^{i\sum_i \eta_{i,p}(l)(c_{i\alpha}^\dagger c_{i\alpha}-\frac{1}{2})}\,|\psi_T^{N_\alpha}\rangle$$
$$\times\prod_{\alpha=N+1}^{2N}\langle\psi_T^{h,N_L-N_\alpha}|\prod_{p=2M}^{1} e^{-\Delta\tau\sum_{i,j}d_{i\alpha}^\dagger K_{ij}d_{j\alpha}} e^{-i\sum_i \eta_{i,p}(l)(d_{i\alpha}^\dagger d_{i\alpha}-\frac{1}{2})}\,|\psi_T^{h,N_L-N_\alpha}\rangle$$
$$\times\left[\prod_{i,p}\gamma_{i,p}(l)\right]. \tag{B13}$$

Now we add back the explicit form of the Slater-determinant states $|\psi_T^{N_\alpha}\rangle$ and $|\psi_T^{h,N_L-N_\alpha}\rangle$ as

$$|\psi_T^{N_\alpha}\rangle = \prod_{j=1}^{N_\alpha}\Big(\sum_{i=1}^{N_L} c_{i\alpha}^\dagger Q_{i,j}^\alpha\Big)|0\rangle = \prod_{j=1}^{N_\alpha}\left(\vec{c}_\alpha^\dagger Q^\alpha\right)_j|0\rangle,$$
$$|\psi_T^{h,N_L-N_\alpha}\rangle = \prod_{j=1}^{N_L-N_\alpha}\Big(\sum_{i=1}^{N_L} d_{i\alpha}^\dagger \tilde{Q}_{ij}^\alpha\Big)|0\rangle_h$$
$$= \prod_{j=1}^{N_L-N_\alpha}\left(\vec{d}_\alpha^\dagger \tilde{Q}^\alpha\right)_j|0\rangle_h, \tag{B14}$$

where $|0\rangle$ and $|0\rangle_h$ are the particle vacuum and hole vacuum states, respectively; N_L is the number of lattice sites; Q_α is a $N_L\times N_\alpha$-dimensional rectangular matrix, and $\tilde{Q}_\alpha$ is a $N_L\times(N_L-N_\alpha)$-dimensional matrix; $\vec{c}_\alpha^\dagger$ and $\vec{d}_\alpha^\dagger$ are vector notations for $c_{i\alpha}^\dagger$ and $d_{i\alpha}^\dagger$ with $i=1$ to N_L.

A Slater-determinant wave function has nice properties as

$$e^{\vec{c}^\dagger M\vec{c}}\prod_{j=1}^{N_p}(\vec{c}^\dagger Q)_j|0\rangle = \prod_{j=1}^{N_p}[\vec{c}^\dagger e^M Q]_j|0\rangle, \tag{B15}$$

and

$$\langle 0|\prod_{j=1}^{N_p}(\vec{c}Q^\dagger)_j\; e^{\vec{c}^\dagger M\vec{c}}\prod_{j=1}^{N_p}(\vec{c}^\dagger Q')_j|0\rangle$$
$$= \det\left[Q^\dagger e^M Q'\right], \tag{B16}$$

where M is an $N_L\times N_L$ Hermitian matrix, or anti-Hermitian matrix.

Based on these properties, we have

$$P_{\{l\}} = \frac{1}{Z}\prod_{\alpha=1}^{N}\det\left[(Q_\alpha)^\dagger\left(\prod_{p=2M}^{1}e^{-K}e^{iV_p(l)}\right)Q_\alpha\right]$$
$$\times\prod_{\alpha=N+1}^{2N}\det\left[\left(\tilde{Q}_\alpha\right)^\dagger\left(\prod_{p=2M}^{1}e^{-K}e^{-iV_p(l)}\right)\tilde{Q}_\alpha\right]$$
$$\times\prod_{i,p}\gamma_{i,p}(l), \tag{B17}$$

where $V_p(l)$ is a purely real diagonal matrix whose i-th diagonal element reads

$$[V_p(l)]_{ii} = \eta_{i,p}(l). \tag{B18}$$

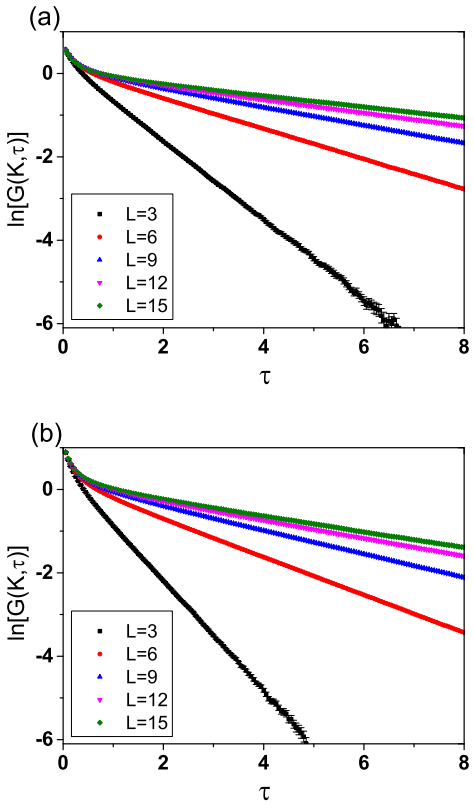

FIG. 17. $\ln G(K,\tau)$ as functions of τ at (a) $U=7$ for SU(4) and (b) $U=11$ for SU(6) at different values of lattice size L. The data are in good quality and the slopes (the Δ_{sp}) are reliably extracted.

If we set the trial wave function to satisfy $N_\alpha = N_L/2$ and thus $Q^{1,\cdots,N} = Q$, $\tilde{Q}^{N+1,\cdots,2N} = Q^*$, then we have

$$P_{\{l\}} = \frac{1}{Z}\left|\det\left[Q^\dagger\left(\prod_{p=2M}^{1}e^{-K}e^{V_p(l)}\right)Q\right]\right|^{2N}$$
$$\times\prod_{i,p}\gamma_{i,p}(l), \tag{B19}$$

thus the probability distribution $P_{\{l\}}$ is positive-definite at half-filling.

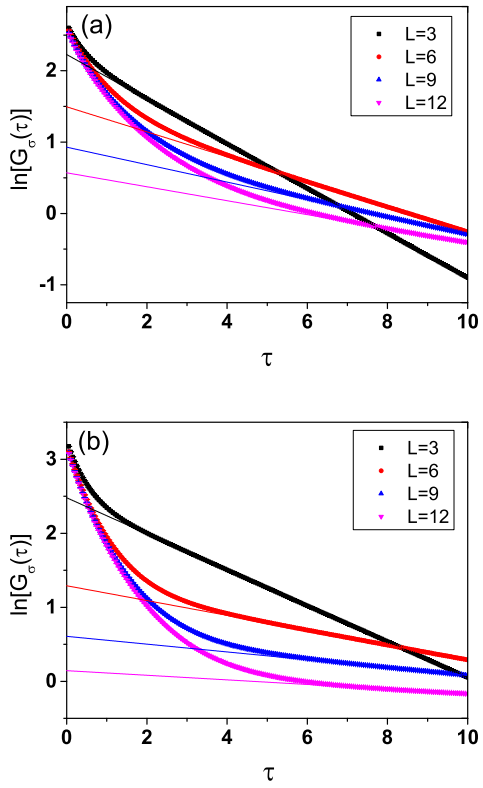

FIG. 18. $\ln G_\sigma(\tau)$ as functions of τ at $U = 6$ for (a) SU(4) and (b) SU(6) at different values of lattice size L. Lines are linear fit whose slopes are the spin gap Δ_σ.

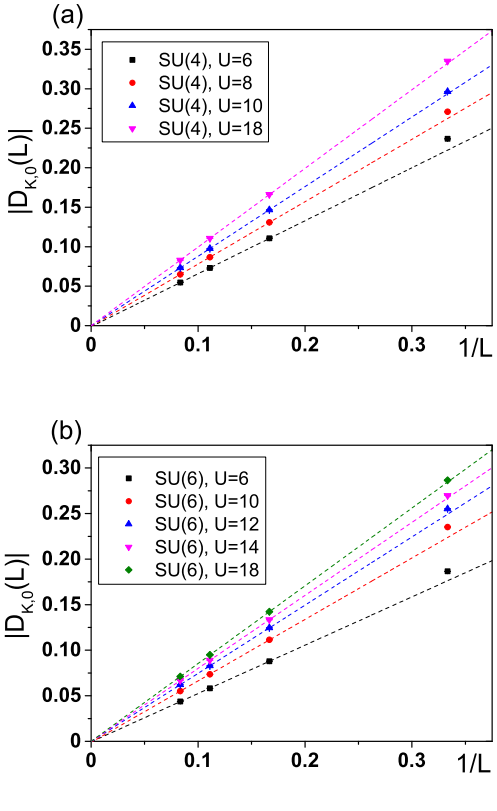

FIG. 19. Finite size scalings of the trimer order parameter for different values of U for (a) the SU(4) case and (b) the SU(6) case. Linear fit is used starting from $L = 6$. Error bars are smaller than the symbol sizes.

Appendix C: Extract the single-particle gap

As discussed in the Sec. III A of the main text, the single-particle gap can be obtained from the imaginary-time displaced Green's function

$$G(K,\tau) = \frac{1}{2L^2}\sum_{i,j\in A\oplus B} G(i,j,\tau)e^{i\vec{K}\cdot(\vec{r}_i-\vec{r}_j)}. \quad \text{(C1)}$$

For long enough τ, according to the Lehmann representation, $G(K,\tau)$ decays in the imaginary time as $\exp(-\Delta_{sp}\tau)$. We can extract the single particle gap Δ_{sp} from the slope of $\ln G(K,\tau)$ vs τ.

In Fig. 17, representative plots of $\ln G(K,\tau)$ versus τ are presented for both the SU(4) and SU(6) cases at $U = 7$ and $U = 11$, respectively. From these plots, we find the linear regime can be easily achieved without large time-displacement in τ, which enables us to extract reliable values of Δ_{sp} shown in the main text.

Appendix D: Extract the spin gap

As discussed in Sec. III B of the main text, the spin gap can be extracted from the imaginary time displaced spin-spin correlation function. Since the leading spin channel instability occurs at the Néel ordering with form factor $(-1)^{i+j}$, we define the spin-spin correlation function as

$$G_\sigma(\tau) = \frac{1}{2L^2}\sum_{i,j,\alpha,\beta}\Big\{(-1)^{i+j}\langle S_{\alpha\beta,i}(\tau)S_{\beta\alpha,j}(0)\rangle\Big\}. \quad \text{(D1)}$$

whose asymptotic behavior at large τ is $G_\sigma(\tau) \sim \exp(-\Delta_\sigma\tau)$. Fig. 18 shows representative data of $\ln G_\sigma(\tau)$ v.s. τ, for both the SU(4) and SU(6) cases, at $U = 6$. The linear regimes at large τ are used to extract the spin gap Δ_σ.

Appendix E: Finite size scaling of trimer and VBS dimer order parameter

For simplicity, we have employed Eq. 9 to calculate the VBS dimer order parameter in the main text by only calculating the correlations among bonds along the same orientations.

We can also use $D_{K,m}$ defined in Eq. 8 to calculate the trimer and the VBS dimer order parameters. The magnitude of the trimer order parameter is defined as

$$|D_{K,0}| = \lim_{L\to\infty}\sqrt{\langle D^*_{K,0}(L)D_{K,0}(L)\rangle}, \quad \text{(E1)}$$

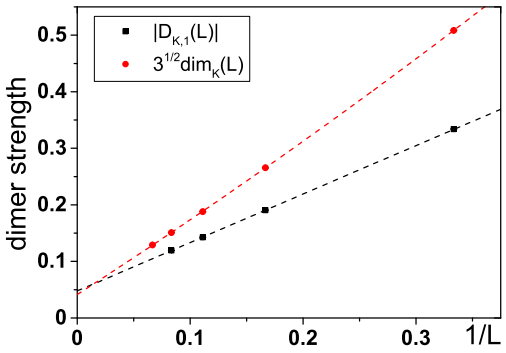

FIG. 20. A comparison of $|D_{K,1}|$ and $\sqrt{3}\mathrm{dim}_K$ with parameters $2N = 4$ and $U = 8$. Linear fit is used from $L = 6$ for $|D_{K,1}(L)|$, and quadratic fit is used from $L = 3$ for $\sqrt{3}\mathrm{dim}_K(L)$.

and $|D_{K,-1}|$ equals to $|D_{K,0}|$. Fig. 19 shows the finite size scaling of the trimer order parameter for both SU(4) and SU(6) cases. Clearly there is no long-range trimer order. The VBS dimer order parameter can also be calculated from the module defined as

$$|D_{K,1}| = \lim_{L\to\infty} \sqrt{\langle D^*_{K,1}(L) D_{K,1}(L)\rangle}. \tag{E2}$$

In the thermodynamic limit, since the trimer correlation is only short-ranged, the relation between $|D_{K,m}|$ and dim_K is

$$|D_{K,1}| = \sqrt{3}\mathrm{dim}_K. \tag{E3}$$

We have compared these two values after the finite-size scaling for a specific parameter in Fig. 20. They matched well in the thermodynamic limit. Then in Fig. 21, the finite size scalings of the VBS dimer order parameter $|D_{K,1}|$ are presented for different U with both SU(4) and SU(6) cases. The phase transition point and the non-monotonic dependence on U are identical comparing with dim_K.

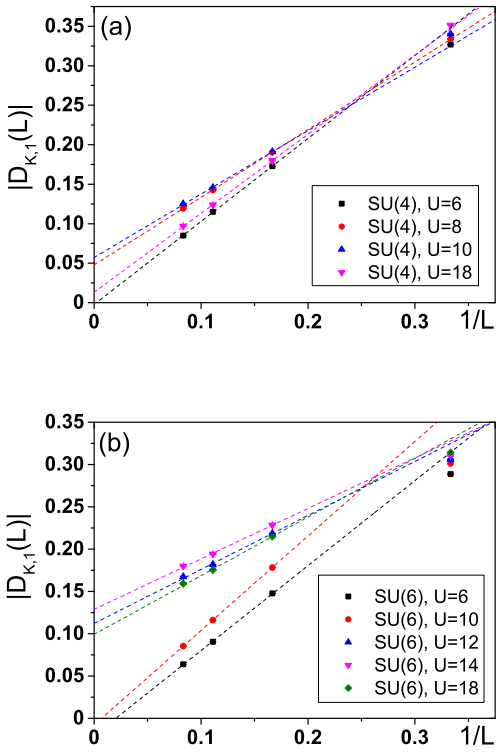

FIG. 21. Finite size scalings of the VBS dimer parameter $|D_{K,1}|$ at different values of U for (a) the SU(4) case and (b) the SU(6) case. The linear fit is starting from $L = 6$, and error bars are smaller than symbols.

Appendix F: Using pinning field method to rule out Néel order

To further clarify whether there is a weak long-range Néel order at large U in the SU(4) case, we employ the pinning field method. Due to its sensitivity to weak Néel order, this method has been applied to the SU(2) Hubbard model in the honeycomb lattice[10] and the SU($2N$) Hubbard model in the square lattice[29]. Following the procedure in Ref. [29], a pinning term is added into the original Hamiltonian Eq. 1 as

$$H_{pin}(i_0, j_0) = h\left[m(i_0) - m(j_0)\right], \tag{F1}$$

in which the onsite magnetic moment is defined as $m(i) = \sum_{\alpha=1}^{N} n_\alpha(i) - \sum_{\alpha=N+1}^{2N} n_\alpha(i)$, and i_0 and j_0 are two nearest-neighbor sites in a unit cell. Since the SU($2N$) symmetry is explicitly broken, the Néel order is induced by the external field. Since the pinning field only applies on two nearest-neighboring sites, and the symmetry breaking effect is at the order of $1/L$. The long-range Néel order is defined as

$$m_Q = \lim_{L\to\infty} \frac{1}{2L^2} \sum_i (-1)^i m(i). \tag{F2}$$

There is only an overall factor difference between M_{nl} in main text and m_Q here in the thermodynamic limit if Néel order actually exists.

We have simulated the Néel ordering for the SU(4) Hubbard model at $U = 16$ and 18 using the pinning field method. $\Delta\tau$ is set as 0.05 after the discrete $\Delta\tau$ scaling. For the pinning field method, much longer projection time is needed because the pinning fields break the SU($2N$) symmetry and thus cause much smaller gap.[10,29] We also performed the scaling over β, and find that very large β (as long as 350) for $L = 12$ is needed to ensure the convergence. The simulation results are presented in Fig. 22, which show the absence of the long-range Néel order for $U = 16$ and 18 in the SU(4) case in consistent with the results in the main text.

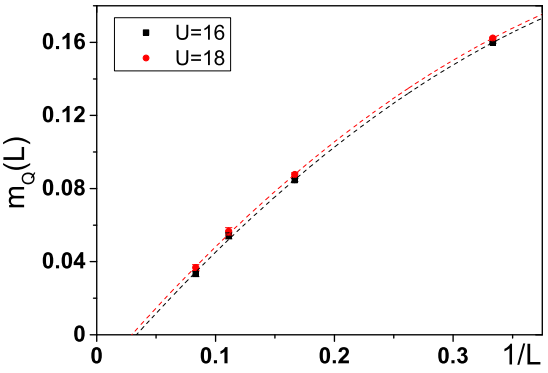

FIG. 22. The absence of Néel order m_Q based on the pinning field method with $U = 16$ and 18 for the SU(4) Hubbard model. The pinning field is $h = 5$. The quadratic polynomial fitting is used, and error bars are smaller than symbols.

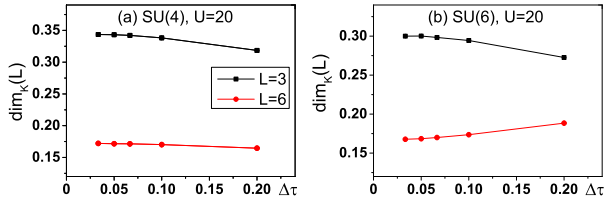

FIG. 23. The scalings of $\Delta\tau$ for the VBS dimer order dim_K. Error bars of QMC data are smaller than symbols.

Appendix G: The discrete $\Delta\tau$ scaling

In this section, we examine the dependence of the QMC results on the imaginary time discretization $\Delta\tau$. Since the discretization error coming from the second-order Suzuki-Trotter decomposition is of order $(\Delta\tau)^3U^2t$, which becomes the most severe when U increases, we only need to check our QMC results at the largest $U = 20$ in our simulations.

We first present the $\Delta\tau$ scalings for the VBS dimer order with $U = 20$ for the SU(4) and SU(6) cases in Fig. 23 (a) and (b), respectively. The data show that $\Delta\tau = 0.05$ is small enough to ensure the convergence, regardless of the lattice size. In Fig. 24 (a) and (b), we further present the $\Delta\tau$ scalings for the Néel order for the SU(4) and SU(6) cases, which also show convergence at $\Delta\tau = 0.05$. Based on these scalings, we use $\Delta\tau = 0.05$ when performing all the QMC simulations in the main text.

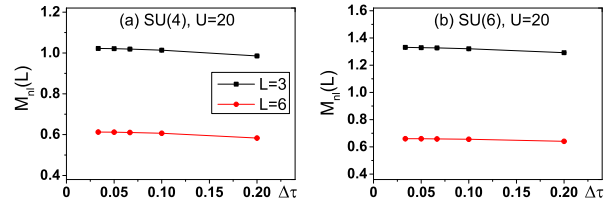

FIG. 24. The scalings of $\Delta\tau$ for the Néel order M_{nl} based on the structure factor. Error bars of QMC data are smaller than symbols.

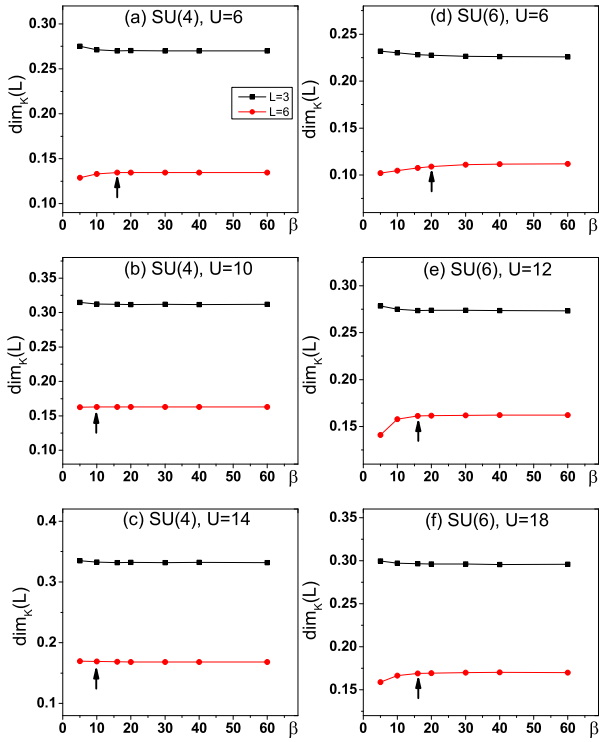

FIG. 25. The scalings of the projection time β for the dimer VBS order dim_K. Arrows denote the β at which the results converge. Error bars of QMC data are smaller than symbols.

Appendix H: The finite β scaling

The projection time β needs to be long enough to arrive at the ground state. For a finite size system with a linear size L, supposing the first excitation gap is $\Delta(L)$, $\exp(-\beta\Delta) \ll 1$ is required. $\Delta(L)$ often scales as $1/L$ with antiferromagnetic correlations. If the system is gapped at $L \to \infty$, $\Delta(L)$ drops to a finite value at sufficiently large values of L. Therefore, we try β proportional to L.

In Fig. 25 (a)- (f), we present the scalings of β for the VBS dimer order parameter for both the SU(4) and SU(6) cases. In each case, three different interactions U are chosen. From the scaling results, we find that

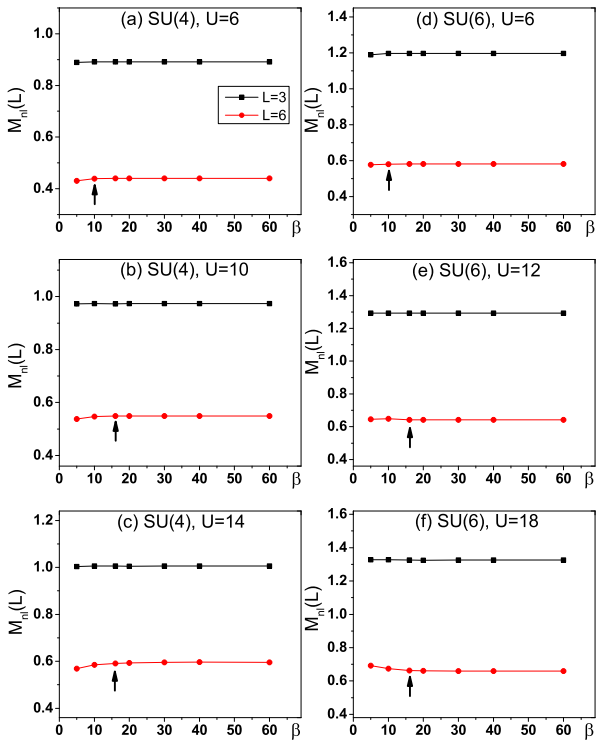

FIG. 26. The scalings of the projection time β for the Néel order M_{nl}. Arrows denote the β at which the results converge. Error bars of QMC data are smaller than symbols.

$\beta = 10 \sim 16$ is enough for convergence for $L = 6$ in most cases, as denoted by the arrows. Therefore, we choose $\beta = 40$ in the simulations to ensure the projection time is long enough to reach the ground states for L up to 15. Similar analyses are performed on the β-dependence of the Néel order parameter in Fig. 26 (a) - (f). We keep choosing the above projection time $\beta = 40$ in all our QMC simulations.

* yu.wang@whu.edu.cn
† wucj@physics.ucsd.edu

[1] A. H. Castro Neto, N. M. R. Peres, K. S. Novoselov, and A. K. Geim, Rev. Mod. Phys. **81**, 109 (2009).
[2] V. N. Kotov, B. Uchoa, V. M. Pereira, F. Guinea, and A. H. Castro Neto, Rev. Mod. Phys. **84**, 1067 (2012).
[3] Z. K. Liu, B. Zhou, Y. Zhang, Z. J. Wang, H. M. Weng, D. Prabhakaran, S.-K. Mo, Z. X. Shen, Z. Fang, X. Dai, Z. Hussain, and Y. L. Chen, Science **343**, 864 (2014).
[4] Z. K. Liu, J. Jiang, B. Zhou, Z. J. Wang, Y. Zhang, H. M. Weng, D. Prabhakaran, S.-K. Mo, H. Peng, P. Dudin, T. Kim, M. Hoesch, Z. Fang, X. Dai, Z. X. Shen, D. L. Feng, Z. Hussain, and Y. L. Chen, Nat. Mater. **13**, 677 (2014).
[5] S. Ryu, C. Mudry, C.-Y. Hou, and C. Chamon, Phys. Rev. B **80**, 205319 (2009).
[6] V. Ayyar and S. Chandrasekharan, Phys. Rev. D **91**, 065035 (2015).
[7] J. Hubbard, Proc. Roy. Soc. London, Ser. A **276**, 238 (1963); Proc. R. Soc. Lond. A **281**, 401 (1964).
[8] Z. Y. Meng, T. C. Lang, S. Wessel, F. F. Assaad, and A. Muramatsu, Nature **464**, 847 (2010).
[9] S. Sorella, Y. Otsuka, and S. Yunoki, Sci. Rep. **2**, 992 (2012).
[10] F. F. Assaad and I. F. Herbut, Phys. Rev. X **3**, 031010 (2013).
[11] I. Affleck and J. B. Marston, Phys. Rev. B **37**, 3774 (1988).
[12] J. P. Lu, Phys. Rev. B **49**, 5687 (1994).
[13] C. Honerkamp and W. Hofstetter, Phys. Rev. Lett. **92**, 170403 (2004).
[14] B. J. DeSalvo *et al.*, Phys. Rev. Lett. **105**, 030402 (2010).
[15] S. Taie *et al.*, Phys. Rev. Lett. **105**, 190401 (2010).
[16] S. Taie, R. Yamazaki, S. Sugawa, and Y. Takahashi, Nat. Phys. **8**, 825 (2012).
[17] X. Zhang, M. Bishof, S. L. Bromley, C. V. Kraus, M. S. Safronova, P. Zoller, A. M. Rey, and J. Ye, Science **345**, 1467 (2014); F. Scazza, C. Hofrichter, M. Hfer, P. C. De Groot, I. Bloch, and S. Flling, Nat. Phys. **10**, 779 (2014); G. Pagano, M. Mancini, G. Cappellini, P. Lombardi, F. Schfer, H. Hu, X.-J. Liu, J. Catani, C. Sias, M. Inguscio, and L. Fallani, Nat. Phys. **10**, 198 (2014).
[18] I. Bloch, J. Dalibard, and W. Zwerger, Rev. Mod. Phys. **80**, 885 (2008).
[19] R. Jördens, N. Strohmaier, K. Günter, H. Moritz, and

T. Esslinger, Nature **455**, 204 (2008).
[20] U. Schneider, L. Hackermüller, S. Will, T. Best, I. Bloch, T. A. Costi, R. W. Helmes, D. Rasch, and A. Rosch, Science **322**, 1520 (2008).
[21] C. Wu, Physics **3**, 92 (2010); Nat. Phys. **8**, 784 (2012).
[22] C. Wu, J.-P. Hu, and S.-C. Zhang, Phys. Rev. Lett. **91**, 186402 (2003).
[23] C. Wu, Phys. Rev. Lett. **95**, 266404 (2005).
[24] K. Hattori, J. Phys. Soc. Jpn. **74**, 3135 (2005).
[25] D. Controzzi and A. M. Tsvelik, Phys. Rev. Lett. **96**, 097205 (2006).
[26] C. Wu, Mod. Phys. Lett. B **20**, 1707 (2006).
[27] Z. Cai, H.-H. Hung, L. Wang, D. Zheng, and C. Wu, Phys. Rev. Lett. **110**, 220401 (2013).
[28] Z. Cai, H.-H. Hung, L. Wang, and C. Wu, Phys. Rev. B **88**, 125108 (2013).
[29] D. Wang, Y. Li, Z. Cai, Z. Zhou, Y. Wang, and C. Wu, Phys. Rev. Lett. **112**, 156403 (2014).
[30] Z. Zhou, Z. Cai, C. Wu, and Y. Wang, Phys. Rev. B **90**, 235139 (2014).
[31] I. Affleck, Phys. Rev. Lett. **54**, 966 (1985).
[32] D. P. Arovas and A. Auerbach, Phys. Rev. B **38**, 316 (1988).
[33] N. Read and S. Sachdev, Phys. Rev. Lett. **62**, 1694 (1989); N. Read and S. Sachdev, Nucl. Phys. B **316**, 609 (1989).
[34] K. Harada, N. Kawashima, and M. Troyer, Phys. Rev. Lett. **90**, 117203 (2003).
[35] N. Kawashima and Y. Tanabe, Phys. Rev. Lett. **98**, 057202 (2007).
[36] A. Paramekanti and J. B. Marston, J. Phys.: Condens. Matter **19**, 125215 (2007).
[37] K. S. D. Beach, F. Alet, M. Mambrini, and S. Capponi, Phys. Rev. B **80**, 184401 (2009).
[38] R. K. Kaul and A. W. Sandvik, Phys. Rev. Lett. **108**, 137201 (2012).
[39] F. Yuan, Q. Yuan, and C. S. Ting, Phys. Rev. B **71**, 104505 (2005).
[40] F. F. Assaad, Phys. Rev. B **71**, 075103 (2005).
[41] T. C. Lang, Z. Y. Meng, A. Muramatsu, S. Wessel, and F. F. Assaad, Phys. Rev. Lett. **111**, 066401 (2013).
[42] L. Tarruell, D. Greif, T. Uehlinger, G. Jotzu, and T. Esslinger, Nature **483**, 302 (2012).
[43] J. E. Hirsch, Phys. Rev. B **31**, 4403 (1985).
[44] S. R. White, D. J. Scalapino, R. L. Sugar, E. Y. Loh, J. E. Gubernatis, and R. T. Scalettar, Phys. Rev. B **40**, 506 (1989).
[45] F. F. Assaad and H. G. Evertz, "Computational many-particle physics," (2008).
[46] S. Pujari, F. Alet, and K. Damle, Phys. Rev. B **91**, 104411 (2015).
[47] F. F. Assaad, ArXiv Condensed Matter e-prints (1998), arXiv:cond-mat/9806307.
[48] F. D. M. Haldane, Phys. Rev. Lett. **61**, 2015 (1988).
[49] C. L. Kane and E. J. Mele, Phys. Rev. Lett. **95**, 226801 (2005).
[50] D. Zheng, G.-M. Zhang, and C. Wu, Phys. Rev. B **84**, 205121 (2011).
[51] Z.-X. Li, Y.-F. Jiang, S.-K. Jian, and H. Yao, arXiv:1512.07908 [cond-mat] (2015), arXiv: 1512.07908.
[52] J. E. Hirsch, Phys. Rev. B **28**, 4059 (1983).